



Microscale reservoir effects on microbial sulfur isotope fractionation

Stilianos Louca^{a,b,*}, Sean A. Crowe^{c,d,*}

^a Biodiversity Research Centre, University of British Columbia, 2212 Main Mall, Vancouver, BC V6T1Z4, Canada

^b Institute of Applied Mathematics, University of British Columbia, 121-1984 Mathematics Road, Vancouver, BC V6T1Z2, Canada

^c Department of Microbiology and Immunology, University of British Columbia, 2.552-2350 Health Sciences Mall, Vancouver, BC V6T1Z3, Canada

^d Department of Earth, Ocean, and Atmospheric Sciences, University of British Columbia, 2207 Main Mall, Vancouver, BC V6T1Z4, Canada

Received 25 September 2016; accepted in revised form 6 January 2017; Available online 14 January 2017

Abstract

Microbial sulfate reduction can impart strong sulfur isotope fractionation by preferentially using the lighter $^{32}\text{SO}_4^{2-}$ over the heavier $^{34}\text{SO}_4^{2-}$. The magnitude of fractionation depends on a number of factors, including ambient concentrations of sulfate and electron donors. Sulfur isotope compositions in sedimentary rocks thus facilitate reconstruction of past environmental conditions, such as seawater sulfate concentrations, primary productivity, organic carbon burial, and sulfur fluxes into or out of the ocean. Knowing the processes that regulate the magnitude of sulfur isotope fractionation is necessary for the correct interpretation of the geological record, but so far theoretical work has focused mostly on internal cellular processes. In sulfate-limited environments, like low sulfate lakes and the Archean ocean, microbial sulfate reduction can lead to sulfate depletion in the water column and an enrichment in isotopically heavy sulfate. This reservoir effect in turn mutes the fractionation expressed in the water column and ultimately preserved in sediments relative to the biologically induced fractionation. Here we use mathematical modeling to show that similar reservoir effects can also appear at the microscale in close proximity to sulfate-reducing cells. These microscale reservoir effects have the potential to modulate sulfur isotope fractionation to a considerable degree, especially at low (micromolar) sulfate concentrations. As a result, background sulfate concentrations, sulfate reduction rates, and extracellular ion diffusion rates can influence the fractionation expressed even if the physiologically induced fractionation is constant. This has implications for the interpretation of biogenic sulfur isotope fractionations expressed in the geological record, because the correct estimation of the environmental conditions that would promote these fractionations requires consideration of microscale reservoir effects. We discuss these implications, and demonstrate the integration of microscale reservoir effects into geobiological models for low sulfate marine water columns, as perceived for the Archean ocean.

© 2017 Elsevier Ltd. All rights reserved.

Keywords: Sulfate reduction; Reservoir effect; Archean ocean; Sulfate gradient; Isotope fractionation

1. INTRODUCTION

Measurements of sulfur (S) isotopes in marine sediments and sedimentary rocks provide a means for reconstructing past changes in the S cycle and, by extension, S isotopes provide a window into the co-evolution of earth surface chemistry and life through time (Canfield and Teske,

Abbreviations: MSR, microbial sulfate reduction; csSRR, cell-specific sulfate reduction rate; AOM, anaerobic oxidation of methane; SMTZ, sulfate–methane transition zone

* Corresponding authors.

E-mail addresses: louca@zoology.ubc.ca (S. Louca), sean.crowe@ubc.ca (S.A. Crowe).

<http://dx.doi.org/10.1016/j.gca.2017.01.007>

0016-7037/© 2017 Elsevier Ltd. All rights reserved.

1996; Canfield, 1998; Canfield et al., 2000; Habicht et al., 2002; Fike and Grotzinger, 2008; Crowe et al., 2014b). Robust reconstructions of the S-cycle from the past, then, depend on an accurate and complete description of factors leading to the deposition and preservation of S isotope signals in sediments. The more detailed our knowledge of the processes that control the magnitude of S isotope fractionation, the more fully we can unpack the wealth of information stored in the geological record (Strauss, 1997). Decades of experimental and theoretical work have shown that by favoring the reaction of ^{32}S relative to ^{34}S , microbial reduction of sulfate to hydrogen sulfide (MSR) has the capacity to impart large S isotope fractionations that approach those expected at thermodynamic equilibrium (^{32}S enrichment up to 66‰; Brunner and Bernasconi, 2005; Canfield et al., 2010a; Sim et al., 2011a). ^{32}S -enriched sulfides can ultimately be preserved as isotopically light S in sedimentary pyrite. Other microbial sulfur metabolisms, such as sulfur disproportionation, also cause large fractionations that can impart additional signals to the geological record (Canfield and Thamdrup, 1994; Canfield and Teske, 1996), whereas abiotic processes like thermochemical sulfate reduction typically impart little fractionation (Machel et al., 1995). Notable exceptions are the photochemical reactions of volcanic SO_2 that take place in the upper atmosphere. These photochemical reactions can impart appreciable S isotope fractionation ($\Delta^{34}\text{S}_{\text{SO}_4\text{-H}_2\text{S}}$) and are also accompanied by a strong mass-independent effect that can be observed through simultaneous measurements of all 4 S isotopes (Farquhar et al., 2000; Savarino et al., 2003). In many cases, however, the overriding control on the S isotopic composition of marine sediments stems from the magnitude of the fractionation imparted as the result of MSR.

Much work has focused on determining the microbial controls on the magnitude of S isotope fractionation during MSR, with most work revealing direct relationships to extracellular sulfate concentrations and inverse relationships to cell specific sulfate reduction rates, all else being equal (Harrison and Thode, 1958; Chambers et al., 1975; Habicht et al., 2002, 2005). More recent work has used quantitative metabolic modeling to show how extracellular sulfate concentrations combine with cellular physiology and electron donor supply to regulate the magnitude of the S isotope fractionation expressed under a given set of conditions (Brunner and Bernasconi, 2005; Johnston et al., 2007; Hoek and Canfield, 2008; Wing and Halevy, 2014). Further physiological work has developed a simplified framework for interpreting the magnitude of expressed S isotope fractionation, based on sulfate uptake affinity and electron donor availability (Bradley et al., 2015). Together, studies to date paint a coherent picture that describes the magnitude of S isotope fractionation expressed during MSR in terms of how open the cell is to sulfate exchange. At one extreme, extracellular sulfate is abundant, electron donor supply is low, and therefore cell-specific sulfate reduction rates are also low. In this case, sulfate is relatively free to exchange into and out of the cell and expressed S isotope fractionations are large (Canfield et al., 2010a; Sim et al., 2011a; Leavitt et al., 2013), possibly approaching the equilibrium fractionation between sulfate and sulfide

($\sim 71\text{‰}$ at 25 °C; Otake et al., 2008) depending on the reversibility of intermediate reactions within the cell. At the other extreme, sulfate concentrations are low, electron donor availability is high and therefore cell-specific sulfate reduction rates are also high. In this case, sulfate has limited exchange into and out of the cell and since sulfate reduction is nearly quantitative, the expressed fractionation is negligible (Sim et al., 2011b; Wing and Halevy, 2014). Any number of intermediate scenarios are also possible, and nutrient limitation or co-limitation can also affect the expressed fractionation (Sim et al., 2011b, 2012). It should be emphasized, however, that specific relationships between sulfate uptake and exchange, electron donor supply, cell-specific sulfate reduction rate and the magnitude of S isotope fractionation are all strain-specific and depend on the relevant enzymatic efficiencies in the organisms involved (Bradley et al., 2015).

Beyond organismal considerations on the magnitude of S isotope fractionation expressed (Kaplan and Rittenberg, 1964; Wing and Halevy, 2014), environmental conditions also play a role in dictating the magnitude of fractionation recorded in sediments. For example, low sulfate conditions or high MSR rates can lead to reservoir effects whereby sulfate concentrations are drawn down leading to the enrichment of the residual sulfate pool in isotopically heavy sulfate (Gomes and Hurtgen, 2013; Crowe et al., 2014b; Gomes and Hurtgen, 2015). Such reservoir effects typically operate to mute the fractionation recorded in sediments (the apparent or expressed fractionation) relative to the magnitude of the induced organismal fractionation (true fractionation). These reservoir effects are typically thought to develop at the basin-scale, where the restriction of water movements, for example through the development of strong vertical density gradients, limits the re-supply of sulfate. A spectacular example of such reservoir effects takes place in Lake Matano, Indonesia, where MSR expresses fractionation above 35‰, but due to sulfate drawdown the fractionations recorded in underlying sediments are on the order of 7.5‰ (Crowe et al., 2014b). Such reservoir effects are common in lakes with low to moderate sulfate concentrations, and may have developed under the low-sulfate marine conditions of the Archean Eon. Similar reservoir effects may also develop at the microscale. For example, it is well known that microorganisms can consume nutrient substrates at rates which cause substrate supply to the cell surface to become diffusion limited (Pasciak and Gavis, 1974). In principle, then, if sulfate supply to cell surfaces becomes diffusion limited, reservoir effects may also develop at the microscale, affecting the expression of S isotope fractionation. In a recent study in marine sediments, Raven et al. (2016) found a surprising 30‰ offset between power water sulfide and pyrite. To explain this offset, the authors proposed that pyrite is formed within microbial aggregates or biofilms, and thus reflects the immediate products of microbial sulfate reduction, in contrast to porewater sulfide, which may be equilibrated with relatively ^{34}S -enriched organic sulfur. Hence, extracellular processes occurring at the microscale can strongly influence the way we interpret ^{34}S signatures in the rock record. Here we modeled extracellular sulfate transport to evaluate the extent to which

microscale reservoir effects might develop and influence S isotope fractionation. We find that such effects can indeed appear and we explore their possible implications for interpreting patterns of S isotope fractionation in laboratory experiments and preserved in the geological record.

2. METHODS

2.1. Overview

We used a partial differential equation based diffusion model to describe extracellular sulfate transport and the concentration gradients that develop in the proximity of single sulfate-reducing cells. We assumed a spherical cell, a homogenous steady sulfate flux across its entire surface and a constant background sulfate concentration and isotopic composition. We solved the time-independent (i.e., steady-state) diffusion equation analytically to obtain solutions for the sulfate profile established as a balance between background sulfate concentrations and sulfate fluxes into the cell. Using the solutions obtained, we calculated the difference between the sulfate S isotopic composition in proximity to the cell (i.e., immediately outside of the cell membrane), when compared to the background composition. This difference, responsible for the reservoir effect discussed below, depends on the diffusion coefficients of the sulfate isotopologues in the surrounding medium, the S isotope fractionation imparted by cellular metabolism, the cell size, sulfate uptake rates, as well as background sulfate concentrations and isotopic compositions. We do not discuss the internal enzymatic mechanisms responsible for cellular S isotope fractionation, but an extensive theoretical literature exists on the topic (Rees, 1973; Brunner and Bernasconi, 2005; Johnston et al., 2007; Wing and Halevy, 2014). Rather, we set cellular isotopic fractionation explicitly. Similarly, we do not discuss specific mechanisms used for trans-membrane sulfate transport (Kertesz, 2001); instead, given a particular sulfate uptake rate, we calculate the corresponding extracellular concentration gradient and the resulting reservoir effect. In addition to the steady-state case, we also solved the time-dependent diffusion equation for the extracellular sulfate profile numerically, in order to examine the transient dynamics of sulfate gradient formation. We then demonstrate how microscale reservoir effects can be incorporated into large-scale geobiological models for S isotope fluxes, using the Archean ocean water column as an example.

2.2. Model derivation

2.2.1. Steady-state extracellular sulfate profiles

In the following, we derive the extracellular sulfate isotopologue gradients that develop under steady-state, when a single spherical sulfate-reducing cell is immersed in a large reservoir of uniform sulfate isotopologue concentrations. Our calculations build on well-established concepts from previous literature on substrate uptake rates by planktonic microorganisms (Purcell, 1977; Koch, 1990, 1996). Under the assumptions stated above, at steady state the extracellular concentration profile of any sulfate isotopologue

satisfies the following partial differential equation (Laplace's equation in spherical coordinates) as a function of radial distance ρ from the cell centre:

$$\frac{1}{\rho^2} \frac{\partial}{\partial \rho} \left(\rho^2 \frac{\partial}{\partial \rho} U_i(\rho) \right) = 0, \quad (1)$$

where i stands for either “32” or “34” depending on the isotopologue, i.e., $U_{32} = [^{32}\text{SO}_4^{2-}]$ and $U_{34} = [^{34}\text{SO}_4^{2-}]$. In addition, U_i satisfies the boundary conditions

$$D_i \frac{\partial}{\partial \rho} U_i \Big|_{\rho=R} = \frac{J_i}{4\pi R^2}, \quad U_i \Big|_{\rho=\infty} = S_i, \quad (2)$$

where R is the cell radius, D_i is the extracellular diffusion coefficient for the isotopologue, J_i is the cell-specific sulfate reduction rate (csSRR) and S_i is the background (i.e., far from the cell) concentration of the isotopologue (symbol overview in Table 1). Solving Eqs. (1) and (2) is straightforward (Evans, 2010) and yields the steady-state extracellular concentration profile

$$U_i(\rho) = S_i - \frac{J_i}{4\pi D_i \rho}. \quad (3)$$

Note that $U_i(\rho)$ decreases as the distance ρ becomes smaller, since diffusion limitation during microbial sulfate reduction leads to the formation of a sulfate-depleted zone around the cell. The steady-state concentration immediately outside of the cell membrane (“near the cell”), henceforth denoted \tilde{S}_i , is obtained from Eq. (3) as $\tilde{S}_i = U_i(R)$, that is:

$$\tilde{S}_i = S_i - \frac{J_i}{4\pi D_i R}. \quad (4)$$

Observe that \tilde{S}_i is established as a balance between sulfate uptake across the cell membrane and supply from the bulk medium. In particular, for smaller cells (smaller R), the same sulfate uptake rates in the same bulk medium would lead to stronger extracellular sulfate gradients and a lower near-cell sulfate concentration \tilde{S}_i . Also note that the above equation implies the existence of an upper bound for the flux J_i , namely $J_i \leq 4\pi D_i R S_i$, above which fluxes cannot be sustained by extracellular diffusion rates (Shaw et al., 2015). This physical limit becomes particularly relevant for prokaryotic cells at low substrate concentrations (Koch, 1996), and does not depend on the nature of transport systems on the cell's membrane.

2.2.2. Induced versus expressed fractionation

In the previous section we derived the steady-state concentration profile for each sulfate isotopologue, as a function of its background concentration (S_i) and its cell-specific reduction rate (J_i), that is, as if S_i and J_i were independently specified. In general, the isotopologue reduction rates J_{32} and J_{34} are tightly coupled and depend on the S isotope fractionation by the cell (i.e. the preferential use of one isotopologue over the other) as well as the near-cell isotopologue concentrations. S isotope fractionation during microbial sulfate reduction is conventionally described by a fractionation factor, α , defined as the ratio of reduced $^{32}\text{SO}_4^{2-}$ over reduced $^{34}\text{SO}_4^{2-}$, divided by the ratio of available $^{32}\text{SO}_4^{2-}$ over available $^{34}\text{SO}_4^{2-}$ (Harrison and

Table 1

Overview of physical variables considered in this study. The subscript i stands for either “32” or “34”, depending on the S isotopologue considered. Ranges are provided for variables that were explicitly set based on literature values.

Symbol	Description	Typical units	Range	Literature
t	time	days		
ρ	distance from cell center	μm		
τ	unit-less time ($\tau = t/(R^2/D)$)	–		
x	unit-less distance from cell center ($x = \rho/R$)	–		
R	cell radius	μm	0.25–1.0	Widdel and Bak (1992) and Nauhaus et al. (2007)
D_i	sulfate diffusion coefficient	m^2/s	$2\text{--}5.6 \times 10^{-10}$	Iversen and Jrgensen (1993)
D_i^*	sulfate transport coefficient for swimming cells, Eq. (42)	m^2/s		
v	cell swimming speed	$\mu\text{m}/\text{s}$	10–600	Fenchel (1994) and Kirboe and Jackson (2001)
$U_i(\rho)$	sulfate isotopologue concentration profile	μM		
J_i	cell-specific sulfate reduction rate (csSRR) per isotopologue	$\text{fmol}/(\text{cell}\cdot\text{day})$		
J	total csSRR	$\text{fmol}/(\text{cell}\cdot\text{day})$		
J_{max}	maximum csSRR	$\text{fmol}/(\text{cell}\cdot\text{day})$	20–200	Detmers et al. (2001)
S_i	background sulfate concentration (per isotopologue)	μM		
S	background sulfate concentration (both isotopologues)	μM	0–100	Habicht et al. (2002)
\tilde{S}_i	near-cell sulfate concentration (per isotopologue)	μM		
\tilde{S}	near-cell sulfate concentration (both isotopologues)	μM		
α	expressed fractionation factor (w.r.t. background sulfate pool)	–		
$\tilde{\alpha}$	induced fractionation factor (w.r.t. near-cell sulfate pool)	–	1.0–1.071	Wing and Halevy (2014)
$\epsilon^{34\text{S}}$	expressed fractionation factor, $\epsilon^{34\text{S}} = (\alpha - 1) \times 10^3$	‰		
$\tilde{\epsilon}^{34\text{S}}$	induced fractionation factor, $\tilde{\epsilon}^{34\text{S}} = (\tilde{\alpha} - 1) \times 10^3$	‰	0–71	Wing and Halevy (2014)
r	background sulfate isotopologue ratio (S_{34}/S_{32})	–	0.0443–0.0457	Lambert et al. (1978) and Shen et al. (2001)
\tilde{r}	near-cell sulfate isotopologue ratio ($\tilde{S}_{34}/\tilde{S}_{32}$)	–		
$\delta^{34\text{S}}$	S isotopic composition (w.r.t. Canyon Diablo Troilite)	‰		
K_h	sulfate half-saturation constant	μM	2–200	Tarpgaard et al. (2011)
$u(\tau, x)$	relative sulfate depletion profile, Eq. (27)	–		
$U^{ss}(\rho)$	steady-state extracellular sulfate concentration profile	μM		
M	auxiliary variable, Eq. (16)	–		
G	auxiliary variable, Eq. (17)	–		
Z	auxiliary variable, Eq. (14)	–		
variables specific to the Archean ocean model (Section 2.5)				
z	water column depth	m		
z_t	minimum considered depth (“top”)	m	100	Crowe et al. (2014b)
z_b	maximum considered depth (“bottom”)	m	250	Crowe et al. (2014b)
r_t	background isotopologue ratio at depth z_t	–	0.0452	Shen et al. (2001, 2008)
S_t	background sulfate concentration at depth z_t	μM	0.05–10	Crowe et al. (2014b)
D	sulfate diffusion coefficient	m^2/s	15.2×10^{-10}	Boudreau (1997) and Robert and Chaussidon (2006)
$V_{max}(z)$	maximum bulk sulfate reduction rate at depth z , also see Table S1	$\mu\text{M}/\text{year}$	0.156–0.864	Crowe et al. (2014b)
$H_i(z)$	bulk sulfate reduction rate at depth z (per isotopologue)	$\mu\text{M}/\text{day}$		
$H(z)$	bulk sulfate reduction rate at depth z (both isotopologues)	$\mu\text{M}/\text{day}$		
K	eddy diffusion coefficient	m^2/day	1.728	Canfield (2006) and Crowe et al. (2014b)
$P_i(z)$	fraction of precipitating sulfide at depth z (per isotopologue)	–		
$N(z)$	cell density of active sulfate reducers at depth z	cells/L		
$\alpha(z)$	expressed fractionation factor at depth z (w.r.t. local background sulfate pool)	–		
Y	proportionality factor between total MSR cells densities and $H(z)$	(cells · days)/mol	1.022×10^{15}	calibrated, see Section 2.5
ϕ	fraction of active MSR cells	–	0.04	Haglund et al. (2002)

Thode, 1958). Hence, α expresses the magnitude for the preferential reduction of the lighter over the heavier isotope, when compared to their relative concentrations. For example, a fractionation factor $\alpha > 1$ means that $^{32}\text{SO}_4^{2-}$ is reduced at a higher proportional rate than would be expected purely based on the background isotopologue ratio, $r = S_{34}/S_{32}$. Fractionation factors are sometimes reported in terms of the relative S^{32} -enrichment in the produced sulfides, $\epsilon^{34}\text{S} (\text{‰}) = (\alpha - 1) \times 10^3$.

The above conventional definition of the fractionation factor does not differentiate between background and near-cell S isotopic composition. In principle, however, isotopic differences in diffusion rates ($D_{32} \neq D_{34}$) and preferential use of $^{32}\text{SO}_4^{2-}$ over $^{34}\text{SO}_4^{2-}$ could lead to a near-cell sulfate S isotopologue ratio, $\tilde{r} = \tilde{S}_{34}/\tilde{S}_{32}$, that is different from that of the background bulk solution:

$$\tilde{r} = \frac{\tilde{S}_{34}}{\tilde{S}_{32}} \neq \frac{S_{34}}{S_{32}} = r. \quad (5)$$

The true (i.e., physiologically induced) fractionation factor, henceforth defined with respect to the near-cell S isotopic sulfate composition,

$$\tilde{\alpha} = \frac{\tilde{S}_{34} \cdot J_{32}}{\tilde{S}_{32} \cdot J_{34}}, \quad (6)$$

will thus generally differ from the apparent or expressed fractionation factor, henceforth defined with respect to the background S isotopic composition:

$$\alpha = \frac{S_{34} \cdot J_{32}}{S_{32} \cdot J_{34}}. \quad (7)$$

In the following, we derive a mathematical relationship between the induced and expressed fractionation factors. Based on the definitions of r and α :

$$S_{32} = \frac{S}{1+r}, \quad S_{34} = \frac{rS}{1+r}, \quad (8)$$

where $S = S_{32} + S_{34}$ is the total background sulfate concentration (ignoring other more rare isotopologues). Similarly,

$$J_{32} = \frac{J}{1+r/\alpha}, \quad J_{34} = \frac{J}{1+\alpha/r}, \quad (9)$$

where $J = J_{32} + J_{34}$ is the total cell-specific sulfate reduction rate. Dividing Eq. (6) by Eq. (7) yields

$$\frac{\tilde{\alpha}}{\alpha} = \frac{\tilde{r}}{r} = \frac{\tilde{S}_{34}}{S_{34}} \cdot \frac{S_{32}}{\tilde{S}_{32}}. \quad (10)$$

Using Eq. (4) in Eq. (10) yields

$$\frac{\tilde{\alpha}}{\alpha} = \frac{1 - \frac{J_{34}}{4\pi D_{34}RS_{34}}}{1 - \frac{J_{32}}{4\pi D_{32}RS_{32}}}. \quad (11)$$

Using Eq. (8) and Eq. (9) in Eq. (11) yields

$$\tilde{\alpha} = \alpha \cdot \frac{1 - \frac{J(1+r)}{4\pi D_{34}RS(\alpha+r)}}{1 - \frac{J\alpha(1+r)}{4\pi D_{32}RS(\alpha+r)}}. \quad (12)$$

Solving Eq. (12) for α yields:

$$\alpha = Z + \frac{1}{2}(\tilde{\alpha} - r) + \sqrt{Z^2 + Z(\tilde{\alpha} - r) + \frac{1}{4}(\tilde{\alpha} + r)^2}, \quad (13)$$

where we denoted:

$$Z = \frac{J}{S} \cdot \frac{(1+r)}{8R\pi D_{32}} \cdot \left(\frac{D_{32}}{D_{34}} - \tilde{\alpha} \right). \quad (14)$$

The formula in Eq. (13) enables the calculation of the expressed fractionation factor α as a function of the induced fractionation factor $\tilde{\alpha}$, provided that R , D_{32} , D_{34} , J , S and r are known. Observe that when Z approaches zero (e.g., for small J), α approaches $\tilde{\alpha}$, as expected.

In order to further elucidate the effects of the isotopologue diffusivities (D_i) and of the induced fractionation ($\tilde{\alpha}$) on α , we derive an alternative formula to Eq. (13), as follows. In analogy to Eq. (12):

$$\alpha = \tilde{\alpha} \cdot \frac{1 + \frac{J(1+\tilde{r})}{4\pi D_{34}RS(\tilde{\alpha}+\tilde{r})}}{1 + \frac{J\tilde{\alpha}(1+\tilde{r})}{4\pi D_{32}RS(\tilde{\alpha}+\tilde{r})}}. \quad (15)$$

To simplify notation, we define the auxiliary variable:

$$M = \frac{\frac{(1+\tilde{r})}{4\pi D_{32}RS(\tilde{\alpha}+\tilde{r})} \cdot \frac{J}{S}}{1 + \frac{\tilde{\alpha}(1+\tilde{r})}{4\pi D_{32}RS(\tilde{\alpha}+\tilde{r})} \cdot \frac{J}{S}} \quad (16)$$

and the variable:

$$G = \left(\frac{D_{32}}{D_{34}} - 1 \right) M - (\tilde{\alpha} - 1)M. \quad (17)$$

Using the definitions (16) and (17), Eq. (15) can now be rewritten in the more compact form:

$$\alpha = \tilde{\alpha} \cdot (1 + G). \quad (18)$$

Note that M is not an independent physical variable, but rather encapsulates the combined effects of multiple factors and is used here merely for representational simplicity (see [Supplemental Fig. S1](#) for typical values of M). The variable G corresponds to the relative deviation of the expressed fractionation factor α from the induced fractionation factor $\tilde{\alpha}$ (“microscale reservoir effect”). In principle, G may be positive or negative and its magnitude corresponds to the strength of the microscale reservoir effect. A positive G corresponds to an amplification of S isotope fractionation, whereas a negative G corresponds to a reduced, or muted fractionation. Importantly, the decomposition in Eq. (17) clarifies that the microscale reservoir effect may generally be caused by two mechanisms, namely isotopic differences in diffusivity ($D_{32} \neq D_{34}$) as well as biogenic fractionation ($\tilde{\alpha} \neq 1$). Since $^{32}\text{SO}_4^{2-}$ is lighter than $^{34}\text{SO}_4^{2-}$, D_{32}/D_{34} is ≥ 1 and $\tilde{\alpha} \geq 1$. The two mechanisms that contribute to a reservoir effect, therefore, act in opposite directions. In particular, a greater diffusivity of $^{32}\text{SO}_4^{2-}$ than $^{34}\text{SO}_4^{2-}$ would facilitate the preferential reduction of $^{32}\text{SO}_4^{2-}$ by the cell, thus increasing the expressed fractionation. Even in the absence of an induced fractionation ($\tilde{\alpha} = 1$), isotopic differences in diffusivity could in principle still lead to an expressed fractionation because near the cell $^{34}\text{SO}_4^{2-}$ would be depleted with respect to $^{32}\text{SO}_4^{2-}$. Such effects have been suggested to occur at the macroscale in marine sediments – where expressed fractionations can be much greater than observed in pure cultures – under the assumption that $D_{32}/D_{34} = \sqrt{98/96}$ according to the theoretical Einstein

relation of diffusion for free ions (Donahue et al., 2008). In reality, however, differences in the diffusivity of $^{34}\text{SO}_4^{2-}$ and $^{32}\text{SO}_4^{2-}$ are likely much lower than predicted by the Einstein relation and negligible compared to the accuracy of contemporary measurements of S isotope fractionation (Bourg, 2008; Wortmann and Chernyavsky, 2011). Water molecules are thought to surround dissolved ions with hydration shells, which likely play an important role in limiting the isotopic differences in diffusion (Richter et al., 2006). Mass isotopic fractionation of ions dissolved in water remains poorly understood, and direct experimental measurements of the diffusion coefficients of $^{34}\text{SO}_4^{2-}$ and $^{32}\text{SO}_4^{2-}$ are clearly needed.

We note that while in this study we focus on the comparison between near-cell and background sulfate S isotopologue ratios (r versus \tilde{r}), our model can also be used to predict the full profile of the sulfate S isotopologue ratio, $[^{34}\text{SO}_4^{2-}]/[^{32}\text{SO}_4^{2-}] = U_{34}/U_{32}$, at any distance ρ from the cell centre. To do so, note that Eqs. (10) and (12) can be combined to give

$$\frac{\tilde{r}}{r} = \frac{1 - \frac{J(1+r)}{4\pi D_{34}RS(z+r)}}{1 - \frac{Jz(1+r)}{4\pi D_{32}RS(z+r)}} \quad (19)$$

Eq. (19) would also hold if R was larger than the actual cell, i.e. corresponding to a hypothetical spherical region around the cell, as long as \tilde{r} is interpreted as the isotopologue ratio at the boundary of that spherical region (i.e. at distance R from the cell centre). Hence, we conclude that the sulfate S isotopologue ratio at any distance ρ from the cell must be given by

$$\frac{U_{34}(\rho)}{U_{32}(\rho)} = \frac{1 - \frac{J(1+r)}{4\pi D_{34}\rho S(z+r)}}{1 - \frac{Jz(1+r)}{4\pi D_{32}\rho S(z+r)}} \quad (20)$$

To illustrate the predictions of the above model (Eq. 13), we visualized the expressed fractionation factor as a function of both the induced fractionation factor and the ratio J/S , for typical marine environments and typical microbial sulfate reducers (Figs. 1 and 2). Specifically, we considered a cell radius $R = 0.25\text{--}0.5 \mu\text{m}$ (Nauhaus et al., 2007) and a sulfate diffusion coefficient (D_{32}) between $2 \times 10^{-10} \text{ m}^2/\text{s}$ and $5.6 \times 10^{-10} \text{ m}^2/\text{s}$, corresponding to values reported for marine sediments and seawater, respectively (Iversen and Jrgensen, 1993; Boudreau, 1997). In all examples, we assumed that S isotopologues have equal diffusivities ($D_{32} = D_{34}$), as discussed above. Unless otherwise stated, in our examples we assumed a standard background sulfate S isotopic composition ($\delta^{34}\text{S} = 0\text{‰}$ relative to Canyon Diablo Troilite, i.e. $r = 0.045005$). However, variations within -15‰ to 15‰ , typical for the Archean ocean (Lambert et al., 1978; Shen et al., 2001), do not significantly affect our results.

2.3. Linking fractionation factors to sulfate concentrations

As shown above in Eq. (14), the microscale reservoir effect explicitly depends both on the csSRR (J) and the background sulfate concentration (S). In natural populations, J and S are correlated variables (Ingvorsen and

Jrgensen, 1984; Pallud and Van Cappellen, 2006) and this correlation must be considered when linking expressed fractionation factors to extracellular sulfate concentrations. The sulfate-dependence of the csSRR is often approximated by a Monod-type function of sulfate concentration (Monod, 1942; Habicht et al., 2002),

$$J = \frac{J_{max} \cdot S}{K_h + S}, \quad (21)$$

with the maximum csSRR, J_{max} , and the half-saturation constant, K_h , being strain-specific or environment-specific parameters. In the following we show how the expressed fractionation factor depends on S when accounting for the interdependence between J and S . Although we use the Monod formula as an example, analogous results may also be obtained using alternative formulas (Boudreau and Westrich, 1984). Using Eq. (21) in Eq. (14) yields the expression

$$Z = \frac{J_{max}}{K_h + S} \cdot \frac{(1+r)}{8R\pi D_{32}} \cdot \left(\frac{D_{32}}{D_{34}} - \tilde{\alpha} \right), \quad (22)$$

which can then be inserted into Eq. (13) to obtain α as a function of S . Observe that in Eq. (22) the rate J is no longer explicitly represented, and hence Z only depends on S and $\tilde{\alpha}$ (in addition to cell-physiological parameters). In particular, for increasing background sulfate concentrations S , Z always eventually approaches 0 and thus the microscale reservoir effect diminishes. In contrast, the lowest expressed fractionation is reached as S approaches zero, and it is determined by the sulfate affinity (i.e., the ratio J_{max}/K_h ; Smith et al., 2009) and is obtained by inserting

$$Z = \frac{J_{max}}{K_h} \cdot \frac{(1+r)}{8R\pi D_{32}} \cdot \left(\frac{D_{32}}{D_{34}} - \tilde{\alpha} \right) \quad (23)$$

into Eq. (13).

To evaluate the above model, we visualized the expressed fractionation factor as a function of S for various realistic physiological scenarios (Fig. 3). We considered half-saturation constants, K_h , ranging from $2 \mu\text{M}$ up to $200 \mu\text{M}$, as reported for various sulfate reducing bacteria (Ingvorsen et al., 1984; Ingvorsen and Jrgensen, 1984; Widdel and Bak, 1992; Sonne-Hansen et al., 1999; Tarpgaard et al., 2011). We chose J_{max} between 20 and $200 \text{ fmol}/(\text{cell}\cdot\text{day})$, according to typical sulfate reduction rates reported by Detmers et al. (2001). We fixed the induced fractionation at the thermodynamic equilibrium fractionation between sulfate and sulfide at 25 °C ($\tilde{\alpha} = 71\text{‰}$; Wing and Halevy, 2014) and considered a cell radius of $R = 0.25 \mu\text{m}$ (Nauhaus et al., 2007).

2.4. Transient dynamics of the extracellular sulfate profile

So far, we have only considered extracellular sulfate gradients and the resulting microscale reservoir effect at steady state. To estimate the spatiotemporal scales involved in the establishment of extracellular sulfate gradients, we explicitly calculate the transient dynamics preceding steady state. Knowledge of the involved time scales, in particular, is needed to assess the suitability of steady-state descriptions in dynamic geochemical settings. In particular, if the

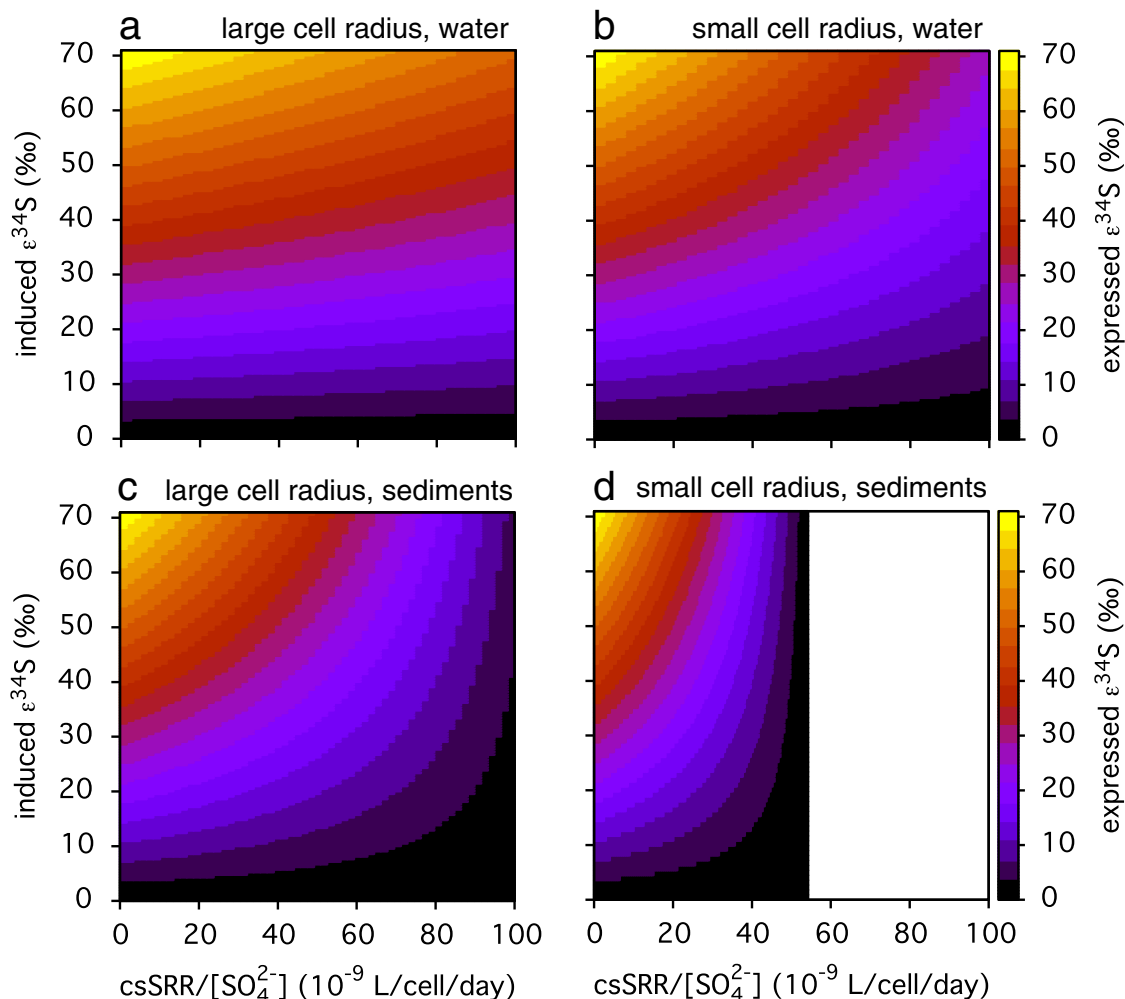


Fig. 1. Expressed (or apparent) fractionation factors for varying induced fractionation factors (vertical axis) and relative cell-specific sulfate reduction rates ($\text{csSRR}/[\text{SO}_4^{2-}]$, horizontal axis), calculated using Eq. (13) in Section 2.2.2. Parameters are a typical diffusion coefficient for water ($D_{32} = D_{34} = 5.6 \times 10^{-10} \text{ m}^2/\text{s}$, top row) and sediments ($D_{32} = D_{34} = 2 \times 10^{-10} \text{ m}^2/\text{s}$, bottom row) (Iversen and Jørgensen, 1993), and a large (left column) and small (right column) cell radius ($R = 0.25\text{--}0.5 \mu\text{m}$; Widdel and Bak, 1992). The white region in (d) corresponds to unrealistically high csSRR, i.e., which exceed the rate sustainable by extracellular diffusive transport.

involved transients are of much shorter duration than typical ecological and geological time scales, then the steady-state formulas derived above can be used in time-dependent geobiological models of microbial S isotope fractionation. Similarly, the spatial scales of sulfate gradients are needed in order estimate the validity of our models for non-spherical cells or for cells with spatially heterogeneous sulfate fluxes (see Discussion). Because the spatiotemporal scales of extracellular sulfate gradient formation by MSR are similar for both isotopologues, and for notational simplicity, we do not differentiate between S isotopologues.

We assume that a sulfate-reducing cell is “introduced” into a medium with homogenous sulfate distribution at time $t = 0$, and we track sulfate concentration profiles as a function of time t and distance ρ from the cell centre. Following the introduction of the cell, the extracellular sulfate

profile, denoted $U(t, \rho)$, behaves according to the diffusion equation in spherical coordinates:

$$\frac{\partial U}{\partial t} = \frac{D}{\rho^2} \frac{\partial}{\partial \rho} \left(\rho^2 \frac{\partial U}{\partial \rho} \right). \quad (24)$$

Note that Eq. (24) is the time-dependent analog to the steady-state Eq. (1). The profile $U(t, \rho)$ satisfies the boundary conditions:

$$U(0, \rho) = S, \quad U(t, \infty) = S, \quad \frac{\partial}{\partial \rho} U(t, R) = \frac{J}{4\pi DR^2}, \quad (25)$$

where S is the background sulfate concentration and J is the csSRR. The steady-state solution of the above diffusion equation was already derived earlier in Eq. (3), and is given by:

$$U^{ss}(\rho) = S - \frac{J}{4\pi D\rho}. \quad (26)$$

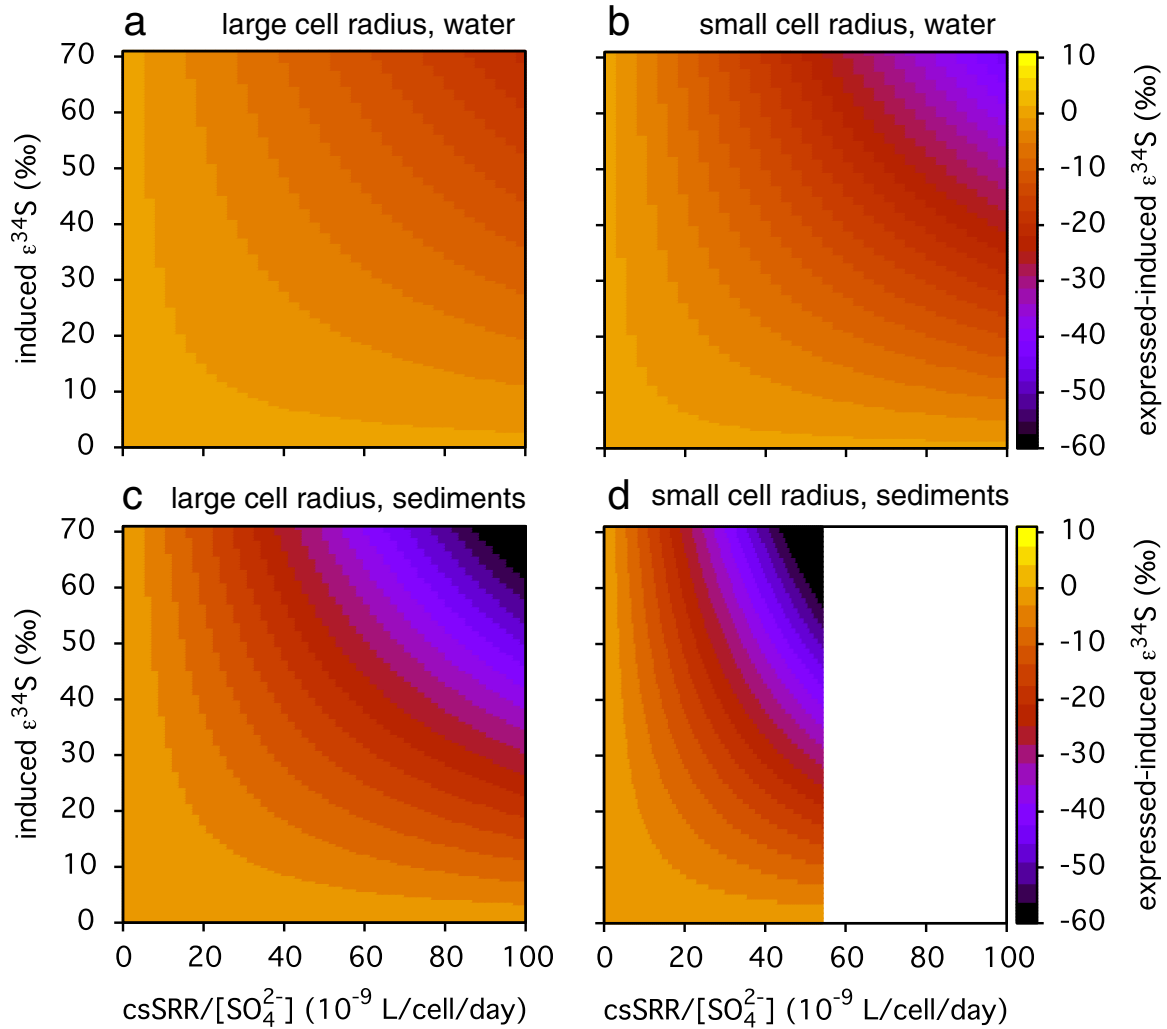


Fig. 2. Difference between expressed and induced fractionation factors for varying induced fractionation factors (vertical axis) and relative cell-specific sulfate reduction rates (csSRR/[SO₄²⁻], horizontal axis), calculated based on Eq. (13) in Section 2.2.2. Parameters are as in Fig. 1, i.e., with a typical diffusion coefficient for water (top row) and sediments (bottom row), and a large (left column) and small (right column) cell radius. The white region in (d) corresponds to unrealistically high csSRR, i.e., which exceed the rate sustainable by extracellular diffusive transport.

The time-dependent profile $U(t, \rho)$ converges to the steady-state $U^{ss}(\rho)$ in the limit $t \rightarrow \infty$. To examine the rate of this convergence, we define the “relative sulfate depletion”:

$$u(t, \rho) = \frac{S - U(t, \rho)}{S - U^{ss}(\rho)}. \quad (27)$$

Note that $u(t, \rho)$ is the difference of the sulfate profile from the background concentration at time t and distance ρ , divided by the steady-state sulfate depletion near the cell. Next, to eliminate redundant parameters, we rescale units by defining $x = \rho/R$ and $\tau = tD/R^2$. Hence, x measures distances from the cell center in terms of cell radii. Similarly, τ measures time in the “characteristic time units” of diffusion, since R^2/D is the time it takes for an initially localized and subsequently diffusing sulfate ion to reach a probability

distribution of variance R^2 . Rewriting the original diffusion equation for $u(\tau, x)$ instead of $U(t, \rho)$ yields the new equation:

$$\frac{\partial u}{\partial \tau} = \frac{1}{x^2} \frac{\partial}{\partial x} \left(x^2 \frac{\partial u}{\partial x} \right) \quad (28)$$

for $x \geq 1$ and $\tau > 0$, with boundary conditions:

$$u(0, x) = 0, \quad u(\tau, \infty) = 0, \quad \frac{\partial}{\partial x} u(\tau, 1) = -1. \quad (29)$$

We solved this new partial differential equation numerically to obtain the relative depletion $u(\tau, x)$ as a function of τ and x . Since the equation is unit-free and parameter-free, the behavior of $u(\tau, x)$ does not depend on any physical or physiological parameters. The dynamics of $u(\tau, x)$ are thus representative for all parameter combinations as long as time, space and sulfate depletion are appropriately

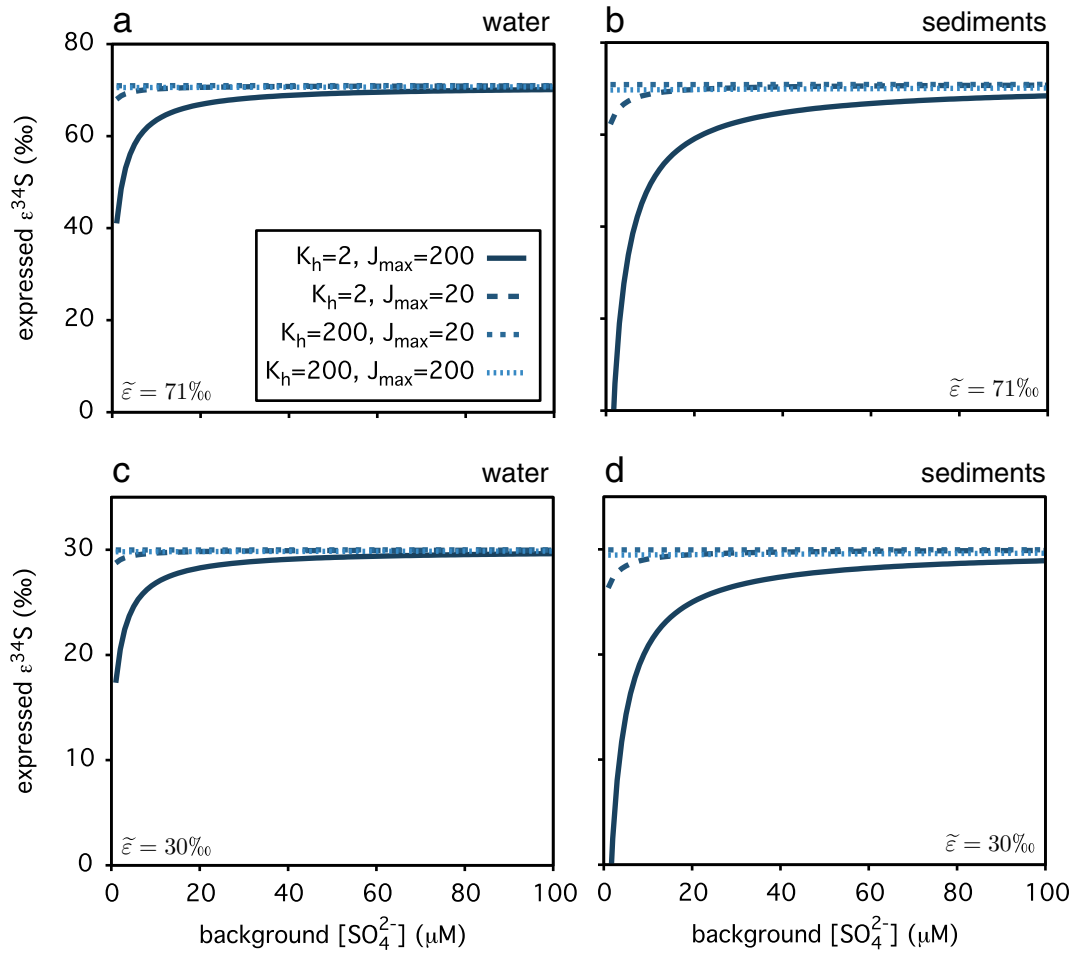


Fig. 3. Expressed (or apparent) fractionation factor over varying background sulfate concentrations when the induced fractionation is fixed at (a, b) $\tilde{\epsilon} = 71\text{‰}$ or (c, d) $\tilde{\epsilon} = 30\text{‰}$, calculated as described in Section 2.3. Sulfate reduction rates are assumed to be Monod functions of sulfate concentrations. Sulfate diffusivities are typical for (a, c) water ($D_{32} = D_{34} = 5.6 \times 10^{-10} \text{ m}^2/\text{s}$) and (b, d) sediments ($D_{32} = D_{34} = 2 \times 10^{-10} \text{ m}^2/\text{s}$). Half-saturation constants (K_h) of sulfate reduction are in μM and maximum cell-specific sulfate reduction rates (J_{max}) are in $\text{fmol}/\text{cell}/\text{day}$.

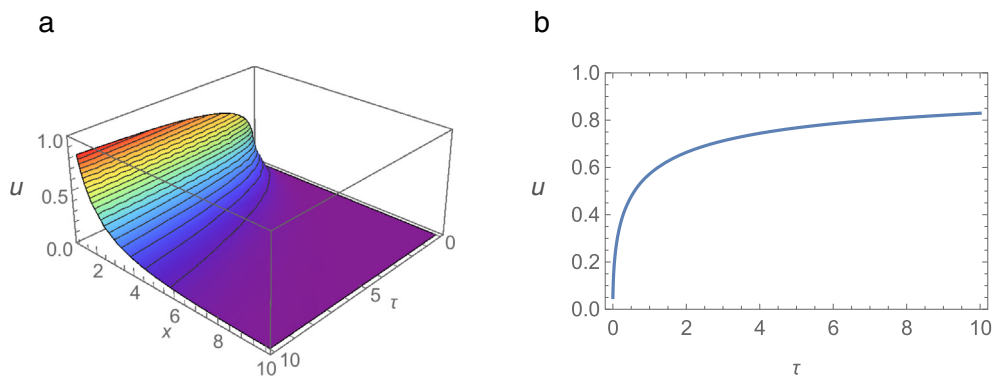


Fig. 4. Transient dynamics of the extracellular sulfate profiles, calculated using Eq. (28) in Section 2.4. (a) Relative sulfate depletion as a function of time (relative to the characteristic time scale R^2/D , i.e. $\tau = t/(R^2/D)$) and distance from the cell centre (relative to the cell radius R , i.e. $x = \rho/R$). Depletion units are relative to the long-term near-cell depletion, and thus range from 0 to 1. Colors correspond to values on the “ u ” axis and are shown for visual aid. (b) Relative sulfate depletion near the cell as a function of time.

interpreted. A visualization of $u(\tau, x)$ over τ and x is provided in Fig. 4a. Further, to evaluate the typical time scales associated with the transients of extracellular sulfate gradients, we consider the rate of change of the relative depletion $u(\tau, x)$ near the cell (i.e., at $x = 1$; Fig. 4b).

2.5. Incorporating microscale reservoir effects in a geobiological model

As we have shown above, the S isotope fractionation expressed by sulfate reducing cells generally depends on multiple factors including the physiologically induced fractionation, extracellular sulfate transport rates, sulfate reduction rates and cell size. These factors need to be considered in geobiological models for S isotope fractionation, in addition to any “macroscale” reservoir effects that may already be incorporated. In the following, we demonstrate how the microscale reservoir effect can be incorporated into conventional steady-state models for S isotope fluxes in a water column or sediment pile. As an example, we use a previous model for S isotope fractionation during microbial sulfate reduction in the Archean ocean water column (Crowe et al., 2014b). This model revealed that under sulfate limitation the expressed fractionation can exhibit strong variation along the water column due to macroscale reservoir effects, even under a constant induced fractionation.

Our starting point is the original 1D reaction–diffusion model for sulfate reduction in the water column (Crowe et al., 2014b). The model assumes that sulfate concentration profiles are determined by microbial sulfate reduction and turbulent (eddy) mixing, according to the following partial differential equation (PDE):

$$\frac{\partial S}{\partial t} = K \frac{\partial^2 S(z)}{\partial z^2} - H(z). \quad (30)$$

Here, $S(z) = [\text{SO}_4^{2-}]$ is the background sulfate concentration at depth z , $H(z)$ is the net bulk sulfate reduction rate and K is the eddy diffusion coefficient. In the model by Crowe et al. (2014b), the rate $H(z)$ corresponds directly to microbial sulfate reduction and depends on $S(z)$ via Monod kinetics:

$$H(z) = \frac{V_{\max}(z)S(z)}{K_h + S(z)}, \quad (31)$$

where $K_h = 5 \mu\text{m}$ is the sulfate half-saturation concentration (Ingvorsen and Jrgensen, 1984; Habicht et al., 2002) and $V_{\max}(z)$ is the maximum SRR at depth z (Table S1). In more general cases, for example in the presence of cryptic sulfur cycling (Canfield et al., 2010b), $H(z)$ would correspond to the difference between sulfate reduction rates and oxidation rates of sulfur compounds to sulfate. Also note that Eq. (30) could include additional sulfate transport terms, for example accounting for vertical advection. Eq. (30) can be solved numerically after setting $\partial S/\partial t = 0$ to obtain the steady-state profiles for $S(z)$ and $H(z)$ (Crowe et al., 2014b).

An incorporation of reservoir effects requires keeping track of the individual background sulfate isotopologue concentrations, $S_{32} = [^{32}\text{SO}_4^{2-}]$ and $S_{34} = [^{34}\text{SO}_4^{2-}]$, across

the water column (Jørgensen, 1979). Specifically, the rate at which each isotopologue is consumed at a particular depth, $H_i(z)$, depends on the total bulk sulfate reduction rate $H(z)$, the fraction of heavy sulfate $S_{34}(z)/S(z)$ and the expressed fractionation $\alpha(z)$. Specifically, according to Eq. (9), the rate of $^{32}\text{SO}_4^{2-}$ consumption is:

$$H_{32}(z) = \frac{H(z)}{1 + (S(z)/S_{32}(z) - 1)/\alpha(z)}, \quad (32)$$

while the rate of $^{34}\text{SO}_4^{2-}$ consumption is:

$$H_{34}(z) = \frac{H(z)}{1 + \alpha(z) \cdot (S(z)/S_{34}(z) - 1)}. \quad (33)$$

Hence, the steady-state profiles $S_{32}(z)$ and $S_{34}(z)$ are the solutions to the reaction–diffusion equations

$$\frac{\partial S_{32}}{\partial t} = K \frac{\partial^2 S_{32}}{\partial z^2} - \frac{H(z)}{1 + (S(z)/S_{32}(z) - 1)/\alpha(z)}, \quad (34)$$

and

$$\frac{\partial S_{34}}{\partial t} = K \frac{\partial^2 S_{34}}{\partial z^2} - \frac{H(z)}{1 + \alpha(z) \cdot (S(z)/S_{34}(z) - 1)}, \quad (35)$$

respectively, after setting $\partial S_{32}/\partial t = 0$ and $\partial S_{34}/\partial t = 0$. Note that, in analogy to the original model by Crowe et al. (2014b) and according to Eq. (8), the profiles S_{32} and S_{34} must also satisfy the boundary conditions

$$S_{32}(z_t) = \frac{S_t}{1 + r_t}, \quad \frac{\partial S_{32}}{\partial z}(z_b) = 0, \quad (36)$$

$$S_{34}(z_t) = \frac{r_t S_t}{1 + r_t}, \quad \frac{\partial S_{34}}{\partial z}(z_b) = 0, \quad (37)$$

where z_t and z_b are the minimum (“top” or “surface”) and maximum (“bottom”) depths of the considered water column, respectively, and r_t and S_t are the fixed isotopologue ratio and fixed sulfate concentration at z_t , respectively. Note that z_t need not correspond to the actual surface and z_b need not correspond to the actual ocean bottom, but instead may define a smaller depth interval that is to be considered in the model, as long as most of the sulfate reduction occurs within that interval.

For the purposes of this example and for parsimony we consider a constant induced fractionation factor $\tilde{\alpha} = 1.03$ (Canfield, 2001; Crowe et al., 2014b); see Supplemental Fig. S6 for a sensitivity analysis and Supplement S3 for a modified model with variable $\tilde{\alpha}$. If microscale reservoir effects are ignored, the expressed $\alpha(z)$ is simply equal to the induced $\tilde{\alpha}$. Such a model, which only accounts for macroscale reservoir effects, is comparable to existing models for S isotope fractionation in sediments (Jørgensen, 1979) or water columns (Crowe et al., 2014b). On the other hand, if microscale reservoir effects are included, the expressed fractionation $\alpha(z)$ differs from $\tilde{\alpha}$ and depends on the sulfate concentration $S(z)$, the csSRR $H(z)/N(z)$ (where N is the density of active sulfate reducers, estimated below), the isotopologue ratio $r(z) = S_{34}(z)/S_{32}(z)$, the cell radius and the sulfate diffusivities (see Eq. 13). Consequently, $\alpha(z)$ itself varies with depth. Note that here macroscale and microscale reservoir effects are associated with two separate sulfate transport processes, namely large-scale turbu-

lent mixing across the water column and diffusion in the proximity of cells, respectively, and thus the corresponding diffusion coefficients must be estimated separately (Table 1). Based on Archean ocean temperature estimates within $\sim 40\text{--}70\text{ }^\circ\text{C}$ (Robert and Chaussidon, 2006) and salinity estimates within $\sim 50\text{--}70\%$ (Knauth, 2005), and using the regression formulas by Boudreau (1997, Table 4.8 and Eq. 4.107) and Sharqawy et al. (2010, Table 5), we estimated sulfate ion diffusion coefficients in Archean seawater within the range $\sim 12.0 \times 10^{-10}\text{--}18.6 \times 10^{-10}\text{ m}^2/\text{s}$. These predicted sulfate diffusivities are substantially higher than diffusivities in typical modern seawater, owing to the high temperatures in the Archean ocean, although these temperatures remain subject to controversy and may have been lower in reality (Hren et al., 2009; Sleep, 2010).

Solving the reaction–diffusion Eq. (35) for $\partial S_{34}/\partial t = 0$ yields the steady-state profile $S_{34}(z)$ and, in combination with Eq. (33), the isotopologue export rate $H_{34}(z)$. Note that since $S(z)$ and $H(z)$ are obtained from Eq. (30), it is sufficient to solve Eq. (35) for $S_{34}(z)$ and $H_{34}(z)$ and then calculate $S_{32}(z)$ and $H_{32}(z)$ through $S_{32} = S - S_{34}$ and $H_{32} = H - H_{34}$. Both the model by Crowe et al. (2014b) and the model considered here, assume that sulfide formation is followed by immediate and quantitative precipitation and sedimentation to the bottom. In anoxic waters, sulfide precipitates abiotically mainly as metal monosulfide crystals, $\text{M}^{2+} + \text{HS}^- \rightarrow \text{MS} + \text{H}^+$ and pyrites, $\text{FeS} + \text{H}_2\text{S} \rightarrow \text{FeS}_2 + \text{H}_2$, where M^{2+} is typically iron (II) or manganese (II) (Rickard, 1997; Lewis, 2010). Given sufficient reactive iron supply, iron sulfidation and pyrite formation can occur very rapidly and quantitatively (Lyons, 1997; Rickard, 1997). Under this scenario, the S isotopic composition of metal monosulfides and pyrites deposited at depth reflects the average S isotopic composition of sulfides produced by MSR in the water column. Hence, once $H_{32}(z)$ and $H_{34}(z)$ are obtained as described above, a summation of the sulfide isotopologue export rates H_{32} and H_{34} across the water column allows predictions for the expected S isotopic composition of sedimentary sulfides:

$$\text{sulfide } \delta^{34}\text{S}(\text{‰}) = \left(\frac{1}{0.045005} \cdot \frac{\int H_{34}(z) dz}{\int H_{32}(z) dz} - 1 \right) \cdot 10^3. \quad (38)$$

We used Eq. (38) to predict the resulting S fractionations in sedimentary sulfides for various imposed surface sulfate levels. We then estimated Archean seawater sulfate levels by comparing the predicted S fractionations to measured fractionations in bulk Archean pyrites, thereby adjusting previous comparisons by Crowe et al. (2014b) to account for microscale reservoir effects.

We note that, in addition to macroscale and microscale reservoir effects during MSR, other geobiological processes potentially affecting sedimentary S fractionation signals may also need to be considered. For example, only a fraction of the produced sulfide may sediment to the bottom due to concurrent sulfide oxidation or iron limitation (Holmer and Storkholm, 2001). Both scenarios appear unlikely in the iron(II)-rich low-oxygen Archean ocean (Crowe et al., 2008, 2014b). In general, however, the fraction of

sulfides precipitating in the water column depends on the availability of reactive iron (II) (Suits and Wilkin, 1998) and on the ability of mixing processes to transport H_2S to the oxic layers before entering the iron catalytic cycle (Ma et al., 2006). To account for this variability, Eq. (38) can be modified to the following:

$$\text{sulfide } \delta^{34}\text{S}(\text{‰}) = \left(\frac{1}{0.045005} \cdot \frac{\int H_{34}(z)P_{34}(z) dz}{\int H_{32}(z)P_{32}(z) dz} - 1 \right) \cdot 10^3. \quad (39)$$

Here, $P_i(z)$ (where i is either “32” or “34”) is the fraction of sulfide produced at depth z that actually sediments to the bottom. Depending on the system examined, the precise shape of $P_i(z)$ may depend on sulfide oxidation rates across the water column or on the extent to which iron limitation affects iron-sulfide precipitation at each depth. In principle, the profile $P_{32}(z)$ may differ from $P_{34}(z)$, for example due to S isotope fractionation upon abiotic metal sulfide precipitation, where metal sulfides become enriched in the lighter ^{32}S . In addition, if pyrite growth is rapid and transport limited (Rickard and Luther, 1997), then a precise prediction of P_{32} and P_{34} may require consideration of microscale reservoir effects during crystal growth. However, experimental and theoretical investigations of precipitation of iron (II) and manganese (II) monosulfides (Ohmoto and Rye, 1979; Böttcher et al., 1998) and pyrite (Price and Shieh, 1979), suggest that S isotope effects during sulfide precipitation are generally small ($\epsilon^{34} \sim 0.2\text{--}1.2\%$) compared to S isotope effects during microbial sulfate reduction.

Here we assumed a diffusion coefficient of $D = 15.2 \times 10^{-10}\text{ m}^2/\text{s}$, corresponding to a middle-range Archean ocean temperature of $55\text{ }^\circ\text{C}$ and salinity of 60% (Knauth, 2005; Robert and Chaussidon, 2006); see Supplemental Fig. S5 for a sensitivity analysis using different D). Similarly to our other examples, we ignored S isotopic differences in sulfate diffusion coefficients, because these differences were likely negligible compared to the induced fractionations considered here (see our discussion in Section 2.2.2 and Richter et al., 2006). We used 5% as a conservative value for surface sulfate $\delta^{34}\text{S}$, i.e. $r_t = 0.0452$ (Shen et al., 2001; Ueno et al., 2008), although this choice did not affect the predicted expressed fractionations (sensitivity analysis in Supplemental Fig. S7). We assumed an MSR cell radius of $R = 0.25\text{ }\mu\text{m}$ (Widdel and Bak, 1992; Nauhaus et al., 2007); for a sensitivity analysis using other radii ($0.25\text{--}1.0\text{ }\mu\text{m}$) see Supplemental Fig. S2.

We estimated the active MSR cell density $N(z)$ by assuming that at steady state $N(z)$ was proportional to the bulk sulfate reduction rate $H(z)$, that is,

$$N(z) = \varphi \cdot Y \cdot H(z), \quad (40)$$

where φ is the fraction of metabolically active MSR cells and Y is a constant proportionality factor (MSR cells \times day per mol substrate). We set $\varphi = 0.04$, according to reported fractions of active pelagic bacteria by Haglund et al. (2002); for a sensitivity analysis using other fractions see Supplemental Fig. S3. The unknown factor Y was calibrated based on total MSR cell densities and bulk

MSR rates measured in Lake Matano, Indonesia (Crowe et al., 2008), as described below. Lake Matano exhibits water column structure and chemistry resembling estimated conditions in the Archean ocean, notably extremely low sulfate concentrations ($< 20 \mu\text{M}$), a permanently anoxic bottom, high ferrous iron concentrations at depth ($\sim 140 \mu\text{M}$) and light penetration well into the anoxic region, and thus serves as a model system for understanding Archean ocean biogeochemistry (Crowe et al., 2008, 2014b). Total cell densities in the Lake Matano water column were determined at a single depth (7.6×10^8 cells/L at 117.5 m in February 2010), which was chosen to be within the region of peak MSR activity (peak sulfate reduction rate 32 nM/day) (Crowe et al., 2014a). Concurrently, environmental DNA shotgun sequences were used to assess the composition of the microbial community at the same depth (data from Crowe et al., 2014a). A total of 1162 16S ribosomal RNA sequences, extracted from the metagenomes, were detected and taxonomically annotated using the MetaPathways platform (Konwar et al., 2013) and the SILVA reference database (release 115; Pruesse et al., 2007) in order to identify the fraction of sulfate reducers in the community. Taxa identified as known sulfate reducers, covering 4.3% of the taxonomically annotated 16S sequences, are summarized in Table S2. Using this approach, we obtained an estimate for the total number of MSR cells (3.27×10^7 cells/L) within the region of peak sulfate reduction, which we divided by the measured sulfate reduction rate in order to calibrate the aforementioned proportionality factor, $Y = (3.27 \times 10^7 \text{ cells/L}) / (32 \text{ nM/day})$. We then used the calibrated Y in Eq. (40) to estimate the active MSR cell densities across the Archean ocean water column, based on the bulk sulfate reduction rates predicted by the reaction–diffusion model, Eqs. (30) and (31). Note that this approach assumes that the cells-per-substrate yields for MSR in the Archean ocean were similar to those in modern Lake Matano. Such an extrapolation, while rather speculative, is currently necessary due to the lack of alternative estimates for MSR cell densities in the Archean ocean water column (for a sensitivity analysis see Supplemental Fig. S4). Future efforts to improve the accuracy of microbial productivity estimates for ancient ecosystems will certainly benefit reconstruction of Earth's elemental cycles.

3. RESULTS

3.1. Induced versus expressed fractionations

The model derived in Section 2.2.2 (Eq. 14) suggests that for a given induced fractionation factor $\tilde{\alpha}$, the expressed fractionation factor only depends on the ratio J/S but not on the individual values of J and S . In particular, Eq. (14) reveals that when sulfate reduction is weak compared to the background sulfate concentration ($J/S \approx 0$), the reservoir effect diminishes and the induced and expressed fractionation factors converge ($\alpha \approx \tilde{\alpha}$). Figs. 1 and 2 show how the expressed S isotope fractionation factor deviates from the induced fractionation factor for varying J/S ratios in water as well as sediments. In general, the reservoir effect

increases when sulfate reduction is strong compared to background sulfate concentrations (high J/S). Further, as seen in Figs. 1 and 2, the reservoir becomes stronger at lower diffusion rates because, all else being equal, lower diffusion rates lead to stronger extracellular sulfate gradients. Consequently, the microscale reservoir effect is expected to be more pronounced in sediments than in the water column. Notably, even at a high induced fractionation of $\tilde{\alpha}^{34\text{S}} \sim 60\text{‰}$, the expressed fractionation can drop down to $\sim 40\text{‰}$ in water (Fig. 1b) and down to $\sim 5\text{‰}$ in sediments (Fig. 1d) when $J/S \sim 50 \text{ nL}/(\text{cell} \cdot \text{day})$.

Our model also predicts that the cell size strongly influences the microscale reservoir effect, which increases in magnitude for smaller cell sizes, all else being equal (Fig. 1 and Eq. 14). For example, within the parameter ranges considered here, at an induced fractionation factor of $\tilde{\alpha}^{34\text{S}} = 60$ the expressed fractionation factor in sediments can be as low as $\sim 35\text{‰}$ for cells of radius $0.5 \mu\text{m}$ and as low as $\sim 5\text{‰}$ for cells of radius $0.25 \mu\text{m}$, when $J/S \sim 50 \text{ nL}/(\text{cell} \cdot \text{day})$. The reason for this sensitivity to cell size is that the increased area-specific sulfate flux for smaller cells leads to a stronger extracellular sulfate gradient, in turn increasing the microscale reservoir effect. Hence, cells with similar sulfate reduction rates and similar enzymatic mechanisms can exhibit markedly different expressed S isotope fractionations merely due to differences in cell size. We note that in general csSRR may depend on cell size and vice versa, and hence the two parameters do not vary independently. For example, many bacteria are known to decrease their cell volume in response to energy limitation, by up to an order of magnitude (Lever et al., 2015).

3.2. Linking fractionation factors to sulfate concentrations

The model derived in Section 2.3 links the expressed fractionation factor to the background sulfate concentration S while accounting for a positive relationship between S and the csSRR J (in terms of Monod kinetics). The derived model suggests that when the induced fractionation ($\tilde{\alpha}$) is constant, the expressed fractionation is a function of S that approaches the induced fractionation with increasing S when S becomes comparable to the half-saturation constant K_h . A similarity between the half-saturating sulfate concentration for sulfate reduction and that for fractionation has indeed been observed in natural populations (Habicht et al., 2002). The expressed fractionation factor is muted more strongly when S is smaller (assuming $\tilde{\alpha} > D_{32}/D_{34}$, Fig. 3). The lowest expressed fractionation, reached as S approaches zero, depends on the sulfate affinity (i.e., the ratio J_{max}/K_h ; Smith et al., 2009), as derived in Eq. (23). Hence, the reservoir effect becomes stronger for cells with higher sulfate affinities when background sulfate concentrations are low. Apart from shaping the magnitude of the reservoir effect, sulfate affinity has also been shown to affect strain-specific induced S isotope fractionation (Bradley et al., 2015). Under certain circumstances (slow diffusion, small cell size and high sulfate affinity) the microscale reservoir effect can lead to a strong positive correlation between sulfate concentrations and the expressed

fractionation, despite a constant induced fractionation (Fig. 3). Similar theoretical predictions have been made for general enzymatically driven reactions coupled to a preceding limiting transport step (Thullner et al., 2008); in that case, and consistent with our conclusions, the sensitivity of the expressed fractionation to the background substrate concentration increases for larger substrate affinities and for smaller transport rate constants.

The microscale reservoir effect is expected to be particularly strong for cells with high sulfate affinities ($J_{max}/K_h > 10$ nL/(cell · day)) in sulfate-limited environments. In the most extreme considered case, i.e., at high affinities $J_{max}/K_h = 100$ nL/(cell · day), the expressed fractionation can become almost completely muted when S falls below a few μM (Fig. 3b). Such severely sulfate-depleted conditions may have existed in the Archean ocean (Habicht et al., 2002; Crowe et al., 2014b), and sulfate reducing bacteria would be expected to be particularly adapted to such conditions, e.g., by exhibiting high sulfate affinities. For example, strains of the ubiquitous sulfate reducer *Desulfovibrio vulgaris* exhibit sulfate half-saturation constants down to $3.3\mu\text{M}$ (Widdel and Bak, 1992; Dalsgaard and Bak, 1994), with reported sulfate reduction rates as high as 180 fmol/(cell · day) ($J_{max}/K_h \approx 55$ nL/(cell · day)). On the other extreme, the reservoir effect becomes negligible when J_{max}/K_h is lower than about 2 nL/(cell · day), as will typically be the case for species with K_h well above $10\mu\text{M}$ or in sulfate-rich environments such as the modern oceans.

3.3. Predicting Archean seawater sulfate levels

The model for S isotope fluxes in the Archean ocean water column, derived in Section 2.5, extends the original model of Crowe et al. (2014b) to account for microscale reservoir effects on MSR. When microscale reservoir effects are ignored, the expressed fractionation factor at each depth is equal to the fixed induced fractionation factor ($\alpha(z) = \tilde{\alpha} = 1.03$; Canfield, 2001; Crowe et al., 2014b). As previously discussed by Crowe et al. (2014b), S isotope

fractionation by MSR then leads to a strong buildup of heavy $^{34}\text{SO}_4^{2-}$ at the bottom (Fig. 5c), and this macroscale reservoir effect mutes the fractionation expressed in the sulfides exported at depth when compared to the surface sulfate pool (sulfide $\delta^{34}\text{S} = -7.5\text{‰}$ at the bottom for a surface sulfate concentration of $1\mu\text{M}$, Fig. 5d). In addition to these effects, our model shows that microscale reservoir effects also mute the expressed fractionation (Fig. 5e), especially at depth, where sulfate is most limited (Fig. 5a). While microscale reservoir effects reduce the buildup of heavy $^{34}\text{SO}_4^{2-}$ at depth (Fig. 5c), overall the fractionation expressed in the exported sulfides is further weakened (sulfide $\delta^{34}\text{S} \sim -5.5\text{‰}$ at the bottom, Fig. 5d).

When microscale reservoir effects are ignored, mean expressed S isotope fractionations in precipitating sulfides ($\Delta^{34}\text{S}_{\text{SO}_4-\text{H}_2\text{S}}$, compared to the surface sulfate pool) are predicted to range from 21.5‰ to 25.2‰ , depending on the assumed surface sulfate concentration ($S_i = 0.05\text{--}10\mu\text{M}$; Fig. 6b). These expressed fractionations are much higher than typical measured fractionations in Archean pyrites (2nd and 3rd quartile $1\text{--}6\text{‰}$, Fig. 6a; Crowe et al., 2014b). Hence, for a constant induced fractionation ($\tilde{\alpha} = 1.03$) and for the considered parameters, without microscale reservoir effects the model fails to reproduce the bulk of measured fractionations, although we note that alternative models with variable $\tilde{\alpha}$ do perform better (Crowe et al., 2014b). In contrast, when microscale reservoir effects are considered, the predicted $\Delta^{34}\text{S}_{\text{SO}_4-\text{H}_2\text{S}}$ ranges from 0‰ (for $S_i \sim 0.05\mu\text{M}$) up to 25‰ (for $S_i \sim 10\mu\text{M}$) (Fig. 6b). A comparison of these predicted mean expressed fractionations to the measured fractionations (Fig. 6a) yields the highest agreement for scenarios with surface sulfate concentrations in the nanomolar range ($\sim 0.05\text{--}0.1\mu\text{M}$). Hence, microscale reservoir effects constitute a possible explanation for the low fractionations expressed in Archean sedimentary pyrites, even under the parsimonious assumption of a constant induced fractionation of 30‰ .

The above predictions are characterized by significant uncertainty, stemming from the model's sensitivity to

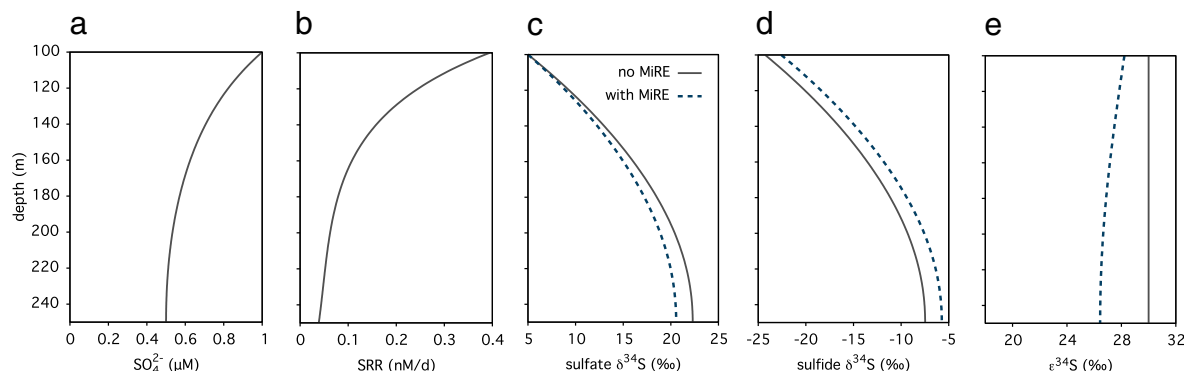


Fig. 5. 1D reaction–diffusion modeling of microbial sulfate reduction and S isotope fractionation in the Archean ocean water column at steady state, as described in Section 2.5. (a) Sulfate concentrations, (b) sulfate reduction rates, (c) sulfate S isotope composition, (d) exported sulfide S isotopic composition, (e) expressed S isotope fractionation (w.r.t. the background sulfate isotopologue composition). Continuous and dashed curves show model predictions without and with the microscale reservoir effect (MiRE), respectively. Sulfate $\delta^{34}\text{S}$ was assumed 5‰ at the surface (Shen et al., 2001), the induced fractionation factor $\tilde{\alpha}$ was fixed at 1.03 and surface sulfate concentration was fixed at $1\mu\text{M}$. For a sensitivity analysis with respect to various model parameters, see Supplemental Fig. S2–S7.

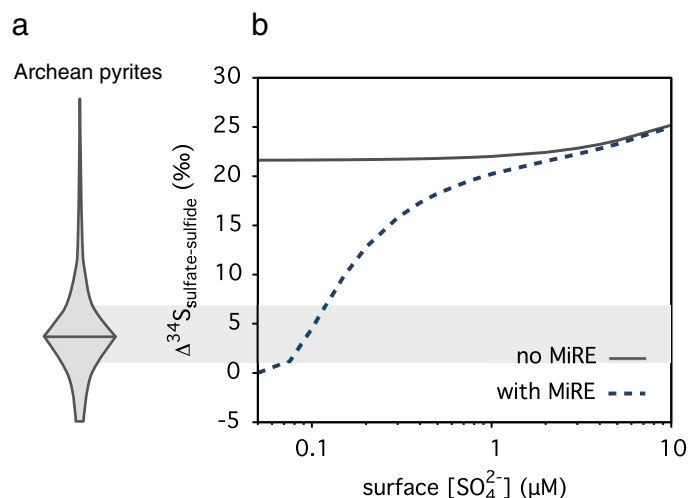


Fig. 6. (a) Distribution of S isotope fractionations expressed in bulk sedimentary Archean pyrites. The horizontal grey band marks the values between the 25% and 75% percentiles. Based on nearly 3000 individual measurements, summarized by Crowe et al. (2014b). (b) Mean expressed S isotope fractionations in sulfides exported across the Archean ocean water column (surface sulfate $\delta^{34}\text{S}$ – deposited pyrite $\delta^{34}\text{S}$), for various imposed surface sulfate concentrations, as predicted by the 1D reaction–diffusion model described in Section 2.5. Continuous and dashed curves show model predictions without and with the microscale reservoir effect (MiRE), respectively. All other model parameters are as in Fig. 5. For a sensitivity analysis with respect to various model parameters, see Supplemental Figs. S2d, S3d, S4d, S5d, S6d, S7d.

poorly known parameters such as MSR cell sizes and active MSR cell densities (and by extension, cell-specific sulfate reduction rates) in the Archean ocean water column. In contrast to the original model of Crowe et al. (2014b) and other geobiological models ignoring microscale reservoir effects (Jørgensen, 1979), these parameters are required for estimating near-cell sulfate depletion and its effects on the expressed fractionations. When we considered alternative cell radii ($R = 0.5\text{--}1.0\ \mu\text{m}$; Widdel and Bak, 1992; Nauhaus et al., 2007), alternative fractions of active MSR cells ($\phi = 0.017\text{--}0.123$; Llobet-Brossa et al., 2002) or alternative cells-per-SRR proportionality factors ($Y = 50\text{--}200\%$ of the calibrated value), we found a significant variation in the predicted depth profiles for sulfate $\delta^{34}\text{S}(z)$ as well as the expressed fractionation $\epsilon^{34}\text{S}(z)$ (Supplemental Fig. S2–S4, respectively). Notably, larger cell radii, higher fractions of active cells and a higher proportionality factor Y (the last two corresponding to lower csSRR, everything else being equal) lead to weaker microscale reservoir effects and to a closer agreement between our model and the original model of Crowe et al. (2014b). Conversely, an increased csSRR (implied by a lower ϕ and/or a lower Y , all else being equal) increases the microscale reservoir effect, thereby leading to substantial deviations from the model of Crowe et al. (2014b). We also observed substantial variation in $\delta^{34}\text{S}(z)$ and $\epsilon^{34}\text{S}(z)$ when we varied the induced fractionation factor ($\tilde{\alpha} = 1.02\text{--}1.04$; Fig. S6), as well as substantial variation in $\delta^{34}\text{S}(z)$ (but not in $\epsilon^{34}\text{S}(z)$) when we varied the S isotopic composition of the surface sulfate pool ($\delta^{34}\text{S} = -15\text{‰}$ to 15‰ ; Lambert et al., 1978; Shen et al., 2001), although this behavior is not surprising and would also be expected for models that ignore microscale reservoir effects. When we considered alternative sulfate ion diffusivities, based on the full range of estimated Archean ocean

temperatures and salinities ($D = 12.0\text{--}18.6 \times 10^{-10}\ \text{m}^2/\text{s}$, see Section 2.5), we observed a much weaker variation in model predictions (Supplemental Fig. S5).

Overall, our sensitivity analysis highlights the need to better understand the population structure and morphological diversity – rather than just bulk reaction-kinetics – of ancient microbial communities. We note that despite significant uncertainties in the predicted depth profiles of $\delta^{34}\text{S}(z)$ and $\epsilon^{34}\text{S}(z)$, the extent of these uncertainties depends on the assumed surface sulfate concentration (S_i). In particular, the predicted fractionation expressed in the deposited pyrites becomes more robust against parameter uncertainty at low S_i (Supplemental Fig. S2–S7). In consequence, it turns out that certain important conclusions from the model remain robust, namely that microscale reservoir effects explain the weak fractionations expressed in the Archean pyrites ($\sim 1\text{--}6\text{‰}$) even under the parsimonious assumption of a constant moderate induced fractionation ($\tilde{\epsilon}^{34}\text{S} = 20, 30$ or 40‰), and that Archean sulfate concentrations may have been as low as $\sim 1\ \mu\text{M}$ (Fig. 6 and Supplemental Fig. S2d–S7d).

3.4. Transient dynamics of the extracellular sulfate profile

The relative sulfate depletion $u(\tau, x)$, derived in Section 2.4 as a function of the rescaled time τ and rescaled distance x from the cell center, yields insight into the transients preceding the establishment of the steady-state extracellular sulfate gradients. Because $u(\tau, x)$ is unit-free and parameter-free, the dynamics of $u(\tau, x)$ are representative for all parameter combinations (e.g., all cell radii R , all possible background sulfate concentrations S , and so on), as long as x is interpreted in terms of cell radii ($x = \rho/R$) and τ is interpreted in terms of “characteristic time units” of

diffusion ($\tau = t/(R^2/D)$). The spatiotemporal profile of $u(\tau, x)$ is shown in Fig. 4a. As can be seen, the extracellular sulfate gradient is characterized by high steepness at the beginning ($\tau \lesssim 1$), with sulfate concentrations dropping from their highest to their lowest value within a distance of less than 2 cell radii ($x \lesssim 2$). Sulfate depletion near the cell proceeds rapidly at first, reaching 50% of its final extent within about 0.6 characteristic diffusion time scales ($0.6 \times R^2/D$), but slows down significantly afterwards (Fig. 4b). For typical cell radii ($R \sim 0.5 \mu\text{m}$) and seawater diffusion rates ($D \sim 5 \times 10^{-10} \text{m}^2/\text{s}$) this corresponds to about 0.3 ms. As the sulfate profile approaches steady state, gradient steepness decreases significantly and extracellular sulfate levels reach background levels within about 5 cell radii ($x \sim 5$). Overall, the spatiotemporal scales of extracellular sulfate gradients are confined within a range of 5 cell radii and reach steady state within only a few characteristic time units (i.e., a few ms).

4. DISCUSSION

4.1. Consequences for geobiological inference

Sulfate concentrations and sulfate reduction rates strongly influence S isotope fractionation during MSR, and hence changes in sedimentary pyrite $\delta^{34}\text{S}$ can yield insight into past sulfate concentrations, sulfate reduction rates and pyrite burial rates (Habicht et al., 2002; Fike and Grotzinger, 2008; Halevy et al., 2012). Because S isotope fractionation by MSR enriches seawater in heavy $^{34}\text{SO}_4^{2-}$ when compared to sulfate input sources (e.g., hydrothermal activity, volcanism or river input), changes in recorded seawater sulfate $\delta^{34}\text{S}$ may also reflect changes of global MSR rates or of S input to the oceans (Paytan et al., 1998). In typical marine sediments MSR is strongly controlled by the amount and reactivity of deposited organic matter (Berner, 1984), thus MSR rates also yield insight into ancient organic carbon fluxes (Strauss, 1997; Fike and Grotzinger, 2008).

Several environmental and physiological factors can affect S isotope fractionation by MSR, and this complicates the robust interpretation of $\delta^{34}\text{S}$ signals in geological records (Strauss, 1997). As shown here, extracellular sulfate transport rates influence the reservoir effect and therefore the expressed fractionation, even if background chemical conditions and cell-physiological characteristics remain unchanged. Hence, theoretical models or calibrations of fractionation as a function of sulfate or electron donor concentration (Habicht et al., 2002; Wing and Halevy, 2014) might not be directly applicable to environments with deviating transport and mixing conditions. In particular, estimates of fractionation obtained from the water column (Crowe et al., 2014b) will potentially misestimate the expressed fractionation in low-sulfate transport-limited environments such as marine sediments, for two reasons. First, the formation of a sulfate-depleted zone near the cell can lead to decreased fractionation due to cellular mechanisms known to induce lower fractionation with decreasing sulfate concentrations (Wing and Halevy, 2014). Cellular

biochemical models only relate S isotope fractionation to near-cell sulfate concentrations, which may differ from the actual background sulfate concentrations. Second, as we have shown, microscale reservoir effects resulting in gradients of S isotopic sulfate composition can further mute fractionation. Ignoring extracellular gradients of sulfate concentration and isotopic composition when interpreting records of expressed fractionation can therefore lead to an underestimation of past sulfate concentrations (Fig. 7) or an overestimation of past MSR rates. Weak expressed S isotope fractionations in marine biogenic pyrites (i.e. high pyrite $\delta^{34}\text{S}$) are sometimes interpreted as a result of macroscale reservoir effects, indicating isolated or semi-isolated marine basins subject to limited exchange of water (and thus sulfate) with the open ocean (Lyons et al., 2000; Luepke and Lyons, 2001). Our work shows that such reservoir effects could have also occurred at the microscale, and hence ^{34}S -enriched marine pyrites need not necessarily reflect a limitation of large-scale sulfate transport.

The presence of microscale reservoir effects does not necessarily compromise the utility of existing models or calibrations of S isotope fractionation, because the cell-physiological information encoded in them can be combined with extracellular transport models to expand their applicability to transport-limited environments (Supplement S1). For example, under the assumptions of this article (purely diffusive transport, spherical cells) the background sulfate concentration can be corrected to account for sulfate depletion near the cell using the approximation:

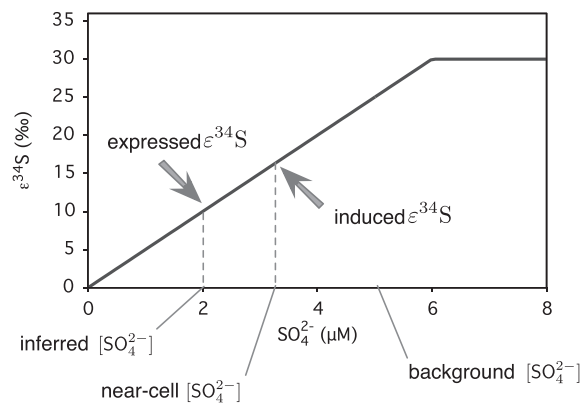


Fig. 7. On the overestimation of expressed S isotope sulfate fractionation in low-sulfate sediments, as discussed in Section 4.1. The linear curve shows a theoretical model of induced fractionation as a function of sulfate concentration $[\text{SO}_4^{2-}]$, based on fractionation data from the water column of an extremely sulfate-depleted lake (Crowe et al., 2014b). At a hypothetical background sulfate concentration of $5 \mu\text{M}$ and a $\text{csSRR} = 100 \text{fmol/cell/d}$, near-cell sulfate concentrations drop to $3.2 \mu\text{M}$ resulting in a reduced induced fractionation (right arrow). Fractionation is further muted due to the microscale reservoir effect (left arrow). An inference of background sulfate concentrations based on the observed expressed fractionation would erroneously yield $[\text{SO}_4^{2-}] = 2 \mu\text{M}$. Parameters in the example are: Diffusion coefficient $D_{34} = D_{32} = 2 \times 10^{-10} \text{m}^2/\text{s}$ (Iversen and Jørgensen, 1993), cell radius $R = 0.25 \mu\text{m}$ (Nauhaus et al., 2007).

$$\tilde{S} \approx S - \frac{J}{4\pi RD_{32}}. \quad (41)$$

For typical cases, i.e., when $D_{32}/D_{34} \approx 1$ and $r \ll \alpha$, the error of this approximation is small when related to the background sulfate level ($|\tilde{S}_{approx} - \tilde{S}_{exact}| \ll S$). The formula becomes exact if the isotopologue diffusivities are equal ($D_{32} = D_{34}$), an assumption that likely applies to sulfate ions in water (Bourg, 2008; Wortmann and Chernyavsky, 2011). The induced fractionation factor $\tilde{\alpha}$ corresponding to \tilde{S} can then be retrieved from the original cellular model, and the expressed fractionation factor α can be estimated using Eq. (13).

Microscale reservoir effects are strongest when sulfate reduction rates are high and sulfate concentrations are low. A negative (positive) correlation between fractionation and csSRR (sulfate concentration) has been widely observed (Harrison and Thode, 1958; Kaplan and Rittenberg, 1964; Chambers et al., 1975) and is typically explained based on intracellular enzyme kinetics (Wing and Halevy, 2014). However, our findings suggest that these observations might partly result from a reservoir effect that modulates an otherwise less variable induced fractionation. Similar effects are well known from previous geobiological models, which show that large-scale gradients in the isotopic composition of SO_4^{2-} can develop due to macroscale reservoir effects even under constant induced fractionations (e.g., at the thermodynamic limit; Crowe et al., 2014b). In general, the observed correlations between sulfate concentrations, sulfate reduction rates, and S isotope fractionations likely result from a combination of microscale reservoir effects and a physiological dependence of the induced fractionation on near-cell concentrations and intracellular fluxes of sulfur compounds (Wing and Halevy, 2014).

Diffusive sulfate transport can be particularly limited in low permeability marine sediments (Strauss, 1997). Accordingly, microscale reservoir effects are expected to be generally more prevalent in sediments than in water columns (Figs. 1c and d), an observation already made for macroscale reservoir effects (Gomes and Hurtgen, 2013; Crowe et al., 2014b). The extent of transport limitation in sediments strongly depends on the tortuosity of the material (Iversen and Jrgensen, 1993). Furthermore, differences in sediment porosity imply differences in the volume of sulfate-bearing water there is to draw from. That said, variation in sediment porosity will typically not affect near-cell sulfate gradients because even at high MSR cell densities ($\sim 10^9$ cells/L; Bak and Pfennig, 1991; Knoblauch et al., 1999), large cell radii ($\sim 1 \mu\text{m}$; Widdel and Bak, 1992) and low porosities ($p \sim 0.1$), the total volume of sulfate reducers still makes up less than 0.01% of the pore water volume.

Our model of the Archean ocean water column demonstrated the potential importance of microscale reservoir effects in large-scale S isotope fractionation patterns, particularly in extremely sulfate limited environments. In such environments, microscale reservoir effects can mute expressed fractionations and thus modulate large-scale gradients in the S isotopic composition of sulfate, which develop as a result of macroscale reservoir effects

(Fig. 5c). Hence, in general, sulfate transport mechanisms both at the micro- as well as macro-scale need to be considered in order to correctly interpret fractionation patterns in the geological record. For example, a comparison of measured fractionations in Archean sedimentary sulfides with fractionations predicted by our models (Fig. 6) shows that estimates for Archean seawater sulfate levels depend not only on the assumed induced fractionation (e.g., constant versus variable; Crowe et al., 2014b), but also on whether microscale reservoir effects are considered. Here we assumed a constant induced fractionation factor $\tilde{\alpha}$ and focused on extracellular sulfate transport processes. In general, intracellular enzymatic processes may also modulate the induced fractionation factor in response to near-cell sulfate concentrations. The extent of this intracellular modulation remains subject to controversy in the theoretical literature (Brunner and Bernasconi, 2005; Wing and Halevy, 2014) and, as we discuss in Sections 2.3 and 3.2, a correlation between expressed fractionation and sulfate concentrations (Harrison and Thode, 1958; Kaplan and Rittenberg, 1964) may partly stem from microscale reservoir effects not considered in previous experiments.

Here we considered steady-state sulfate concentration and fractionation profiles across the Archean ocean water column, as well as the resulting average fractionations expressed in the pyrite formed. While the assumption of a steady state simplified our simulations, an incorporation of microscale reservoir effects need not be limited to steady-state geobiological models. As we have shown, the near-cell sulfate gradients that are responsible for the microscale reservoir effect develop within a few milliseconds (Section 3.4). The involved transients are thus of negligible duration compared to typical ecological and geological time scales. Hence, our formulas linking local sulfate concentrations and sulfate reduction rates to induced and expressed fractionations (e.g., Eqs. 17 and 13) can all be incorporated into more complex, time-dependent geobiological models. Such dynamical models can also account for macroscale reservoir effects with slow transients or dynamic sediment deposition processes (Crowe et al., 2014b). Furthermore, time-dependent models may account for temporal averaging of geological records, a frequent caveat in many geological and paleontological studies (Fürsich and Aberhan, 1990; Kowalewski and Bambach, 2008), by integrating predicted variables over time prior to comparison with data.

We point out that even if the inclusion of the microscale reservoir effect in a geobiological model is mathematically straightforward, several physiological and ecological parameters (e.g., cell densities, cell sizes and diffusion coefficients) are required to make predictions for specific cases, possibly increasing model uncertainties. For example, as explained in Section 2.5, active MSR cell densities for our Archean ocean model were estimated by extrapolating modern cell counts and molecular data from Lake Matano, an Archean ocean analog (Crowe et al., 2008). Our sensitivity analysis revealed that model predictions strongly depend on these estimates, because uncertainties in cell densities (at any given bulk sulfate reduction rate) lead to uncertainties in estimated csSRR. Hence, the increased accuracy that is theoretically attainable by our model, comes at the price

of a dependency on additional and so far largely unexplored parameters. Furthermore, care must be taken when predicting physiological responses and enzyme kinetics in ancient extreme environments (e.g., at 40–70 °C temperature during the Archean) based on current understanding of extant sulfate reducers. For example, shifts in the activation energies of sequential reactions at high temperatures may lead to deviations from experimental and theoretical predictions of induced fractionations (Habicht et al., 2002; Wing and Halevy, 2014). In conclusion, more accurate reconstruction of ancient sulfur cycling will require a better physiological and ecological characterization of sulfate reducing communities in natural ecosystems, particularly in environments resembling ancient conditions.

The model derived in Section 2.2 predicts the sulfate concentration profile (Eq. (2)) and S isotopic composition profile (Eq. (20)) around sulfate reducing cells. Testing these predictions experimentally would require the measurement of sulfate concentrations and S isotopic compositions around active cells at nanoscale to microscale resolution. Nanoscale secondary ion mass spectrometry (nanoSIMS) allows measurement of S isotopic composition at such scales (Herrmann et al., 2007). NanoSIMS has been used previously to detect substantial variation in S isotopic composition between adjacent pyrite grains in ca. 3400 Ma old sandstone, with both $\delta^{34}\text{S}$ and $\Delta^{33}\text{S}$ (where $\Delta^{33}\text{S} = \delta^{33}\text{S} - 0.515\delta^{34}\text{S}$) spanning negative and positive values at spatial scales as small as $\sim 5 \mu\text{m}$ (Wacey et al., 2010). This variation between individual pyrite grains, especially in the sign of $\Delta^{33}\text{S}$, indicates a co-occurrence of multiple sulfur metabolic pathways (microbial sulfate reduction and microbial sulfur disproportionation) in close proximity (Wacey et al., 2010). Note that while our model predicts the establishment of an extracellular gradient of sulfate $\delta^{34}\text{S}$ (as a balance between near-cell and background $\delta^{34}\text{S}$, Eq. (20)), this is not the case for exported sulfide (and thus subsequently formed pyrite). All sulfide exported by a single cell is predicted to exhibit the same isotopic composition, namely corresponding to the expressed fractionation α . Hence, microscale reservoir effects of sulfate reduction by a single cell would not cause heterogeneities in $\delta^{34}\text{S}$ within pyrite grains like in the sulfate pool. Consistent with this expectation, individual μm -sized pyrite grains – presumably formed around single cells, were found to exhibit constant isotopic composition (Wacey et al., 2010, Fig. 2 therein). In contrast, substantial variation in $\delta^{34}\text{S}$ was found even between pyrite grains that presumably all originated from microbial sulfate reduction ($\delta^{34}\text{S}$ from -11.7 to 0 and $\Delta^{33}\text{S} < 0$; Wacey et al., 2010). This variation in expressed fractionation between (but not within) pyrite grains may reflect a modulation by microscale reservoir effects (e.g., depending on cell or colony size), or it may reflect a variation of the induced fractionation between individual cells.

Strong gradients in sulfide $\delta^{34}\text{S}$ have been observed within pyrite crystals at scales ~ 50 – $100 \mu\text{m}$ in borehole waters, with pyrite $\delta^{34}\text{S}$ increasing towards the rim of the crystals (Drake et al., 2015). These gradients suggest almost-closed-system conditions within the crystals due to limited sulfate diffusion from the bulk fluid, causing an

enrichment in heavy sulfate and thus the production of heavier sulfides towards the interior (Drake et al., 2015). This reservoir effect, which forms due to an enrichment in $^{34}\text{SO}_4^{2-}$ at scales spanning multiple cells, is comparable to “macroscale” reservoir effects in isolated or semi-isolated basins (Lyons et al., 2000; Gomes and Hurtgen, 2013; Crowe et al., 2014b) and should not be confused with the microscale reservoir effect modeled here, which occurs due to $^{34}\text{SO}_4^{2-}$ enrichment in the immediate proximity of single cells. Only the former actually results in μm -scale gradients in the precipitating pyrite $\delta^{34}\text{S}$.

4.2. Reservoir effects in sulfate–methane transition zones

Sulfate reduction can be coupled to the anaerobic oxidation of methane (AOM) by syntrophic microbial consortia in or near sulfate–methane transition zones (SMTZ), where upward diffusing methane produced at depth intersects with sulfate diffusing from the overlying water column (Orphan et al., 2001; Hinrichs and Boetius, 2003; Harrison et al., 2009). The bulk of sulfate reduction coupled to AOM is typically confined to within the SMTZ (Hinrichs and Boetius, 2003), although weak sulfate reduction – potentially sustained by cryptic sulfur cycling – can also occur below the SMTZ at low (~ 50 – $400 \mu\text{M}$) “residual” sulfate levels (Holmkvist et al., 2011; Treude et al., 2014). In modern marine environments, where ocean surface sulfate levels are around 28 mM and rates of sulfate reduction are controlled by low-affinity ($K_h \sim 0.2 \text{ mM}$) sulfate reducers (Habicht et al., 2002; Tarpgaard et al., 2011), sulfate rarely drops below $\sim 0.5 \text{ mM}$ within the SMTZ (Devol et al., 1984; Orphan et al., 2001; Harrison et al., 2009; Webster et al., 2011). Microscale reservoir effects, as predicted by our model, will thus have little effect on the fractionation expressed in modern marine SMTZs (Fig. 3). In freshwater lake sediments, where sulfate levels in the micromolar range select for high sulfate affinities ($K_h \sim 5$ – $30 \mu\text{M}$; Ingvorsen and Jørgensen, 1984), diagenetic sulfate reduction can occur at much lower sulfate concentrations (~ 3 – $30 \mu\text{M}$; Herlihy and Mills, 1985; Hordijk et al., 1985; Lovley and Klug, 1983; Lovley and Klug, 1986; Kuivila et al., 1989; Holmer and Storkholm, 2001) and hence microscale reservoir effects of S isotope fractionation may be more important in these environments. It is possible that micromolar sulfate levels in the Archean ocean (Crowe et al., 2014b) would have selected for marine sulfate reducers with high sulfate affinities ($K_h < 5 \mu\text{M}$) similar to modern freshwater systems (Tarpgaard et al., 2011). Consequently, Archean marine SMTZs may have been characterized by lower sulfate levels and significant microscale reservoir effects, if AOM-based syntrophy had evolved by then.

We emphasize that while microscale reservoir effects are predicted to be negligible in modern – and perhaps Archean – marine SMTZs, macroscale reservoir effects of S isotope fractionation may still occur during AOM in diffusion-limited systems at cm-scales due to local enrichment in isotopically heavy sulfate (Jørgensen, 1979). Macroscale and microscale reservoir effects can be incorporated into existing diagenetic models of SMTZs (Devol et al., 1984) in the same way as demonstrated in Section 2.5 for the

Archean water column. An incorporation of microscale reservoir effects requires knowledge of MSR cell sizes and of cell-specific – rather than bulk – sulfate reduction rates, however existing studies of SMTZs rarely consider these additional variables. Our work suggests that microscale reservoir effects may be (or may have been) important in some SMTZs, and that an understanding of S isotope fractionation in these cases requires more detailed characterization of the involved microbial communities than was done so far.

4.3. Can motility mitigate the reservoir effect?

Cell motility is known to enhance nutrient uptake by eukaryotic phytoplankton by overcoming diffusion-limited transport to the cell (Pasciak and Gavis, 1974). For smaller organisms such as prokaryotes, the effects of motility are often much weaker (Guasto et al., 2012). Several sulfate reducers are motile (Castro et al., 2000), hence the question arises whether their motion could reduce the microscale reservoir effect of S isotope fractionation. In analogy to Pasciak's and Gavis's work, our mathematical results can be modified to account for cell movement at some constant speed v by replacing each diffusion coefficient, e.g., D_{32} , with a transport coefficient,

$$D_{32}^* = D_{32} \left(1 + \frac{Rv}{2D_{32}} \right). \quad (42)$$

The ratio Rv/D_{32} is known as the Péclet number, and measures the relative importance of advective transport compared to diffusive transport over the cell's length scale (Karp-Boss et al., 1996). Eq. (42) is only an approximation that becomes valid for small Péclet numbers (Acrivos and Taylor, 1962). The transport coefficient increases with cell speed and cell size. In particular, cell movement has the same effect as increased diffusion and would, in principle, result in a weaker reservoir effect. The magnitude of cell speeds that can significantly alter the reservoir effect becomes apparent in Eq. (42): $v \approx D_{32}/R$ approximately marks the threshold above which the transport coefficients differ significantly from the pure diffusion coefficients. For most cell radii (typically $<1 \mu\text{m}$; Widdel and Bak, 1992) and sulfate diffusion rates $D_{32} \approx 5.6 \times 10^{-10} \text{ m}^2/\text{s}$ in seawater (Iversen and Jørgensen, 1993), this means that swimming speeds below $500 \mu\text{m}/\text{s}$ are unsubstantial.

Typical prokaryote swimming speeds range within 10–100 $\mu\text{m}/\text{s}$, but speeds up to 400–600 $\mu\text{m}/\text{s}$ have also been reported (Fenchel, 1994; Magariyama et al., 1995; Mitchell et al., 1995a; Mitchell and Barbara, 1999; Kirboe and Jackson, 2001). Sinking speeds of free-living prokaryotes are typically well below 300 $\mu\text{m}/\text{s}$ (Fennel et al., 2006). Hence, motion of sulfate reducing cells is not expected to noticeably affect the reservoir effect. As seen in Fig. 8 for typical sulfate reducers in seawater, even a swimming velocity of 500 $\mu\text{m}/\text{s}$ only slightly affects the reservoir effect, when compared to the non-motile case. This is in contrast to Pasciak's and Gavis's findings of significant effects of cell motility on nutrient uptake by flagellated phytoplankton (Pasciak and Gavis, 1974). However, cell sizes considered by Pasciak and Gavis are 1–2 orders of

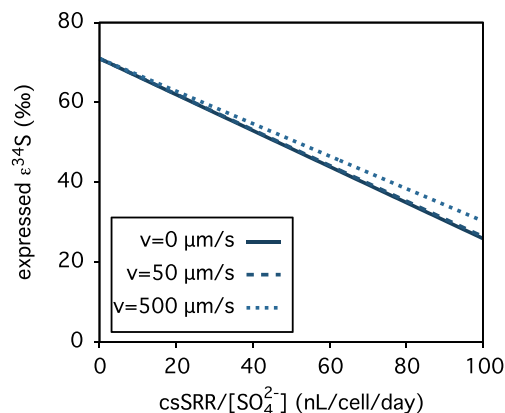


Fig. 8. Expressed fractionation factor over varying relative cell-specific sulfate reduction rates ($\text{csSRR}/[\text{SO}_4^{2-}]$) for motile cells of various speeds, calculated as described in Section 4.3. Parameters are a typical diffusion coefficient for water, $D_{32} = 5.6 \times 10^{-10} \text{ m}^2/\text{s}$ (Iversen and Jørgensen, 1993), and a small cell radius, $R = 0.25 \mu\text{m}$ (Nauhaus et al., 2007). The induced fractionation factor was fixed to the thermodynamic limit at 25 °C, i.e. 71‰ (Otake et al., 2008).

magnitude greater than those of typical sulfate reducing prokaryotes, which explains the greater effects found therein.

In principle, our analysis of the effects of cell movement only apply to steady-state conditions established at constant swimming speeds. Flagellated bacteria can exhibit strong movement bursts and sudden changes in swimming direction (e.g., run-and-tumble movements), possibly allowing them to keep track of localized nutrient sources (Mitchell et al., 1995b,a). However, as we have shown, the sulfate-depleted zone surrounding a cell forms within time scales characteristic of sulfate ion diffusion (R^2/D) and extends to a distance of about 5 cell radii. For typical cell radii ($R \sim 0.5 \mu\text{m}$) and seawater diffusion rates ($D \sim 5 \times 10^{-10} \text{ m}^2/\text{s}$), even rapid movement bursts of up to 600 $\mu\text{m}/\text{s}$ would only propel a sulfate reducer by about 0.6 cell radii within the time it takes for the re-establishment of the sulfate-depleted zone. Hence, typical flagellum-enabled motion, either steady or abrupt, would not be sufficient to completely escape the sulfate-depleted zone and to overcome the microscale reservoir effect.

This conclusion is consistent with theoretical calculations that predict negligible effects of flow or swimming on nutrient uptake rates by organisms smaller than 10 μm (Purcell, 1977; Karp-Boss et al., 1996; Guasto et al., 2012). Furthermore, the characteristic scale of gradients resulting from turbulent mixing in water (the “Batchelor scale”, which in the sea ranges between 30 and 300 μm) is typically much larger than typical MSR cells (Stocker, 2012). At the scale of individual MSR cells, viscous forces eliminate turbulence, and sulfate transport is dominated by molecular diffusion rather than advection (Fenchel, 2002). Consequently, while turbulent mixing (e.g., in a stirred bioreactor or in the ocean water column) can accelerate sulfate transport at ecosystem scales, turbulent mixing has negligible effects on extracellular sulfate gradients in the vicinity of a cell (Purcell, 1977; Koch, 1990; Fenchel,

2002). Hence, microscale reservoir effects are expected to occur even in well-mixed environments.

4.4. Relaxing assumptions

As we have shown, microscale reservoir effects of S isotope fractionation result from the combination of two simple and common processes: (a) the formation of extracellular sulfate gradients in the proximity of sulfate reducing cells due to transport limitation and (b) differences in the magnitude of these gradients between S isotopologues due to the preferential use of particular isotopologues by cells and, potentially, different isotopologue diffusivities. Hence, reservoir effects are generally expected to be most prevalent in sulfate-poor environments subject to strong transport limitation, such as in freshwater lake sediments with low permeability. The quantitative relationships derived here provide guidance on the expected magnitude of microscale reservoir effects and the relative importance of various environmental and physiological factors.

We point out, however, that sulfate reducing bacteria can take many non-spherical shapes (Castro et al., 2000). Sulfate gradients around non-spherical cells will typically be weaker than for spherical cells due to higher surface-area-to-volume ratios. Hence, reservoir effects for non-spherical cells are expected to be weaker than predicted here. For example, approximation formulas for sulfate concentrations around long cylindrical cells suggest that near-cell sulfate depletion for rod-shaped cells typically ranges within 75–105% of the spherical case (at equal cell volume, see Supplement S2 for derivation). However, for extremely thin and elongated (e.g., filamentous) organisms (e.g., *Desulfonema* spp.; Fukui et al., 1999) sulfate gradients can disappear, hence eliminating any microscale reservoir effects. Extreme cases like these will require special considerations, and experimental work may be needed to determine sulfate gradients and reservoir effects if theoretical estimates are not available.

In addition, transmembrane sulfate fluxes may deviate from the homogenous distribution assumed here, particularly in cells with structural membrane inhomogeneities such as flagella (Zhilina et al., 1997) or uneven active transporter distribution. These inhomogeneities will, in turn, lead to inhomogeneities in extracellular near-cell sulfate concentrations. That said, as shown above, sulfate gradients around a cell typically extend to about 5 cell radii. Hence, if inhomogeneities in transmembrane fluxes span across scales much smaller than the cell, sulfate depletion will be roughly constant across the periphery of the cell. If larger inhomogeneities are suspected, our formulas should only be used as rough estimates.

Any formulas predicting microscale reservoir effects for individual cells, including the ones presented here, will inevitably depend on particular physiological and morphological properties. Natural microbial communities can include several sulfate reducing species with different metabolic efficiencies, sizes and shapes (Leloup et al., 2009). For example, a single environment can host a variety of MSR morphotypes, such as thin rods and vibrios (Amann

et al., 1992) or cocci and rods (Ravenschlag et al., 2000), and sulfate reducers with vastly different sulfate affinities have been shown to coexist in marine sediments (Tarpgaard et al., 2011). Hence, sulfate reduction kinetics and expressed fractionations may need to be averaged over members of a community, based on the morphological and physiological variation estimated for a particular environment. Existing experimental calibrations of S isotope fractionation by sulfate reducers focus on pure cultures or engineered systems (Habicht et al., 2002), however our work shows that a characterization of MSR community structure (both kinetic and morphological) in natural environments may be necessary for correctly interpreting S isotope fractionation signals in the geological record; this remains an area for future research. Fluorescence in situ hybridization may be used to estimate size and shape distributions in MSR communities (Amann et al., 1992; Ravenschlag et al., 2000). To estimate the distribution of sulfate reduction kinetics, complementary incubation experiments targeting different substrate regimes may be performed, or composite models (i.e. containing multiple kinetic components) may be fitted to measured progress curves (Tarpgaard et al., 2011).

In our calculations we assumed that sulfate transport in the proximity of individual sulfate reducing cells is captured by the bulk sulfate diffusion coefficients in the medium. In reality, however, the relevant diffusion coefficients for bacteria living in sediments depends on the location of the cells relative to small-scale material structures, i.e. on whether cells are floating in the pore spaces, are attached to surfaces, reside inside detrital particles or are part of a biofilm. For example, oxygen diffusion coefficients have been shown to be reduced by one third inside biofilms of sewage fermenters, when compared to the bulk medium (Tomlinson and Snaddon, 1966). Hence, while here we used bulk diffusion coefficients for our examples, in some cases diffusion coefficients will need to be adjusted to the material (e.g., particulate organic matter, extracellular polymeric substances) immediately surrounding sulfate reducing cells. In most cases, diffusion in the immediate proximity of cells will be slower than in the bulk medium (Tomlinson and Snaddon, 1966; Jørgensen, 1977; Stewart, 2003), and hence microscale reservoir effects will be stronger than predicted here. Microelectrode techniques may be used to determine diffusion coefficients inside individual particles or within biofilms (Revsbech and Jørgensen, 1986; Nishina et al., 1997). More generally, a better understanding of the ecology and spatial structuring of MSR communities is needed for correctly interpreting S fractionation signals in the rock record.

5. CONCLUSIONS

Microscale sulfate concentration gradients can develop between cell surfaces and bulk solutions as a result of microbial sulfate reduction. The magnitude of this concentration gradient depends on cell-specific sulfate reduction rates and the transport properties of the surrounding solutions. Cell-specific sulfate reduction rates are, in turn, influenced by electron donor availability and cell physiology, in

particular the specific affinity for sulfate – high specific affinities lead to strong gradients, all else being equal. A difference in the S isotopic composition of sulfate across this gradient develops mainly as a result of enzymatic isotope discrimination by sulfate reducers as well as, potentially, differing diffusion rates of sulfate isotopologues. This reservoir effect needs to be considered when relating measured isotope fractionations to bulk solution properties such as sulfate concentration, since the true isotope fractionation induced during reduction can be muted, resulting in a measured effective fractionation that includes microscale reservoir effects. Here we focused on S isotope fractionation during microbial sulfate reduction, however microscale reservoir effects potentially also influence isotopic signals of microbial activity on other elements such as carbon, nitrogen or iron (Delwiche and Steyn, 1970; Barker and Fritz, 1981; Brantley et al., 2001).

It should be noted that microscale reservoir effects become particularly relevant at micromolar sulfate concentrations. Such low concentrations are uncommon in modern marine environments (François and Gérard, 1986; Holmer and Storkholm, 2001), but were likely typical in the Archean ocean (Crowe et al., 2014b). Furthermore, media with low permeability and poor mixing will generally result in much stronger extracellular sulfate gradients, and hence microscale reservoir effects are expected to be more prevalent in sediments when compared to the water column (Iversen and Jørgensen, 1993). The models reported here can be used to identify scenarios with significant microscale reservoir effects and to potentially correct for these effects when interpreting observed S isotope fractionations. Such corrections should allow more meaningful and robust comparisons of S isotope fractionation patterns determined in different systems where microscale reservoir effects might be divergent.

ACKNOWLEDGEMENTS

This work was inspired through discussion with Bo Barker Jørgensen. Boswell Wing is thanked for helpful comments. S.L. acknowledges the financial support of the PIMS IGTC for Mathematical Biology as well as the Department of Mathematics, UBC. Research was also supported through an NSERC discovery grant to S.A.C.

APPENDIX A. SUPPLEMENTARY DATA

Supplementary data associated with this article can be found, in the online version, at <http://dx.doi.org/10.1016/j.gca.2017.01.007>.

REFERENCES

- Acrivos A. and Taylor T. D. (1962) Heat and mass transfer from single spheres in stokes flow. *Phys. Fluids* **5**, 387–394.
- Amann R. I., Stromley J., Devereux R., Key R. and Stahl D. A. (1992) Molecular and microscopic identification of sulfate-reducing bacteria in multispecies biofilms. *Appl. Environ. Microbiol.* **58**, 614–623.
- Bak F. and Pfennig N. (1991) Sulfate-reducing bacteria in littoral sediment of Lake Constance. *FEMS Microbiol. Lett.* **85**, 43–52.
- Barker J. F. and Fritz P. (1981) Carbon isotope fractionation during microbial methane oxidation. *Nature* **293**, 289–291.
- Berner R. A. (1984) Sedimentary pyrite formation: An update. *Geochim. Cosmochim. Acta* **48**, 605–615.
- Böttcher M. E., Smock A. M. and Cypionka H. (1998) Sulfur isotope fractionation during experimental precipitation of iron (II) and manganese(II) sulfide at room temperature. *Chem. Geol.* **146**, 127–134.
- Boudreau B. P. (1997) *Diagenetic models and their implementation; modelling transport and reactions in aquatic sediments*. Springer.
- Boudreau B. P. and Westrich J. T. (1984) The dependence of bacterial sulfate reduction on sulfate concentration in marine sediments. *Geochim. Cosmochim. Acta* **48**, 2503–2516.
- Bourg I. C. (2008) Comment on “modeling sulfur isotope fractionation and differential diffusion during sulfate reduction in sediments of the Cariaco basin” by M.A. Donahue, J.P. Werne, C. Meile and T.W. Lyons. *Geochim. Cosmochim. Acta* **72**, 5852–5854.
- Bradley A. S., Leavitt W. D., Schmidt M., Knoll A. H., Girguis P. R. and Johnston D. T. (2015) Patterns of sulfur isotope fractionation during microbial sulfate reduction. *Geobiology* **14**, 91–101.
- Brantley S. L., Liermann L. and Bullen T. D. (2001) Fractionation of Fe isotopes by soil microbes and organic acids. *Geology* **29**, 535–538.
- Brunner B. and Bernasconi S. M. (2005) A revised isotope fractionation model for dissimilatory sulfate reduction in sulfate reducing bacteria. *Geochim. Cosmochim. Acta* **69**, 4759–4771.
- Canfield D. E. (1998) A new model for Proterozoic ocean chemistry. *Nature* **396**, 450–453.
- Canfield D. E. (2001) Isotope fractionation by natural populations of sulfate-reducing bacteria. *Geochim. Cosmochim. Acta* **65**, 1117–1124.
- Canfield D. E. (2006) Models of oxic respiration, denitrification and sulfate reduction in zones of coastal upwelling. *Geochim. Cosmochim. Acta* **70**, 5753–5765.
- Canfield D. E. and Teske A. (1996) Late Proterozoic rise in atmospheric oxygen concentration inferred from phylogenetic and sulphur-isotope studies. *Nature* **382**, 127–132.
- Canfield D. and Thamdrup B. (1994) The production of 34S-depleted sulfide during bacterial disproportionation of elemental sulfur. *Science* **266**, 1973–1975.
- Canfield D. E., Habicht K. S. and Thamdrup B. (2000) The Archean sulfur cycle and the early history of atmospheric oxygen. *Science* **288**, 658–661.
- Canfield D. E., Farquhar J. and Zerkle A. L. (2010a) High isotope fractionations during sulfate reduction in a low-sulfate euxinic ocean analog. *Geology* **38**, 415–418.
- Canfield D. E., Stewart F. J., Thamdrup B., De Brabandere L., Dalsgaard T., Delong E. F., Revsbech N. P. and Ulloa O. (2010b) A cryptic sulfur cycle in oxygen-minimum-zone waters off the Chilean coast. *Science* **330**, 1375–1378.
- Castro H. F., Williams N. H. and Ogram A. (2000) Phylogeny of sulfate-reducing bacteria. *FEMS Microbiol. Ecol.* **31**, 1–9.
- Chambers L. A., Trudinger P. A., Smith J. W. and Burns M. S. (1975) Fractionation of sulfur isotopes by continuous cultures of *Desulfovibrio desulfuricans*. *Can. J. Microbiol.* **21**, 1602–1607.
- Crowe S. A., Jones C., Katsev S., Magen C., O'Neill A. H., Sturm A., Canfield D. E., Haffner G. D., Mucci A., Sundby B. and Fowle D. A. (2008) Photoferrotrophs thrive in an Archean Ocean analogue. *Proc. Natl. Acad. Sci. USA* **105**, 15938–15943.
- Crowe S. A., Maresca J. A., Jones C., Sturm A., Henny C., Fowle D. A., Cox R. P., Delong E. F. and Canfield D. E. (2014a)

- Deep-water anoxygenic photosynthesis in a ferruginous chemocline. *Geobiology* **12**, 322–339.
- Crowe S. A., Paris G., Katsev S., Jones C., Kim S. T., Zerkle A. L., Nomosatryo S., Fowle D. A., Adkins J. F. and Sessions A. L., et al. (2014b) Sulfate was a trace constituent of Archean seawater. *Science* **346**, 735–739.
- Dalsgaard T. and Bak F. (1994) Nitrate reduction in a sulfate-reducing bacterium, *Desulfobrevibrio desulfuricans*, isolated from rice paddy soil: Sulfide inhibition, kinetics, and regulation. *Appl. Environ. Microbiol.* **60**, 291–297.
- Delwiche C. C. and Steyn P. L. (1970) Nitrogen isotope fractionation in soils and microbial reactions. *Environ. Sci. Technol.* **4**, 929–935.
- Detmers J., Brüchert V., Habicht K. S. and Kuever J. (2001) Diversity of sulfur isotope fractionations by sulfate-reducing prokaryotes. *Appl. Environ. Microbiol.* **67**, 888–894.
- Devol A. H., Anderson J. J., Kuivila K. and Murray J. W. (1984) A model for coupled sulfate reduction and methane oxidation in the sediments of Saanich Inlet. *Geochim. Cosmochim. Acta* **48**, 993–1004.
- Donahue M. A., Werne J. P., Meile C. and Lyons T. W. (2008) Modeling sulfur isotope fractionation and differential diffusion during sulfate reduction in sediments of the Cariaco basin. *Geochim. Cosmochim. Acta* **72**, 2287–2297.
- Drake H., Tullborg E. L., Whitehouse M., Sandberg B., Blomfeldt T. and Åström M. E. (2015) Extreme fractionation and micro-scale variation of sulphur isotopes during bacterial sulphate reduction in deep groundwater systems. *Geochim. Cosmochim. Acta* **161**, 1–18.
- Evans L. (2010) *Partial Differential Equations. Graduate Studies in Mathematics*, 2nd ed. American Mathematical Society.
- Farquhar J., Bao H. and Thiemens M. (2000) Atmospheric influence of earth's earliest sulfur cycle. *Science* **289**, 756–758.
- Fenchel T. (1994) Motility and chemosensory behaviour of the sulphur bacterium *Thiovulum majus*. *Microbiology* **140**, 3109–3116.
- Fenchel T. (2002) Microbial behavior in a heterogeneous world. *Science* **296**, 1068–1071.
- Fennel K., Wilkin J., Levin J., Moisan J., O'Reilly J. and Haidvogel D. (2006) Nitrogen cycling in the Middle Atlantic Bight: results from a three-dimensional model and implications for the North Atlantic nitrogen budget. *Global Biogeochem. Cycles* **20**.
- Fike D. A. and Grotzinger J. P. (2008) A paired sulfate–pyrite $\delta^{34}\text{S}$ approach to understanding the evolution of the Ediacaran–Cambrian sulfur cycle. *Geochim. Cosmochim. Acta* **72**, 2636–2648.
- François L. M. and Gérard J. C. (1986) A numerical model of the evolution of ocean sulfate and sedimentary sulfur during the last 800 million years. *Geochim. Cosmochim. Acta* **50**, 2289–2302.
- Fukui M., Teske A., Amus B., Muyzer G. and Widdel F. (1999) Physiology, phylogenetic relationships, and ecology of filamentous sulfate-reducing bacteria (genus *Desulfonema*). *Arch. Microbiol.* **172**, 193–203.
- Fürsich F. T. and Aberhan M. (1990) Significance of time-averaging for palaeocommunity analysis. *Lethaia* **23**, 143–152.
- Gomes M. L. and Hurtgen M. T. (2013) Sulfur isotope systematics of a euxinic, low-sulfate lake: evaluating the importance of the reservoir effect in modern and ancient oceans. *Geology* **41**, 663–666.
- Gomes M. L. and Hurtgen M. T. (2015) Sulfur isotope fractionation in modern euxinic systems: Implications for paleoenvironmental reconstructions of paired sulfate–sulfide isotope records. *Geochim. Cosmochim. Acta* **157**, 39–55.
- Guasto J. S., Rusconi R. and Stocker R. (2012) Fluid mechanics of planktonic microorganisms. *Annu. Rev. Fluid Mech.* **44**, 373–400.
- Habicht K. S., Gade M., Thamdrup B., Berg P. and Canfield D. E. (2002) Calibration of sulfate levels in the Archean ocean. *Science* **298**, 2372–2374.
- Habicht K. S., Salling L., Thamdrup B. and Canfield D. E. (2005) Effect of low sulfate concentrations on lactate oxidation and isotope fractionation during sulfate reduction by *Archaeoglobus fulgidus* strain z. *Appl. Environ. Microbiol.* **71**, 3770–3777.
- Haglund A. L., Törnblom E., Boström B. and Tranvik L. (2002) Large differences in the fraction of active bacteria in plankton, sediments, and biofilm. *Microb. Ecol.* **43**, 232–241.
- Halevy I., Peters S. E. and Fischer W. W. (2012) Sulfate burial constraints on the Phanerozoic sulfur cycle. *Science* **337**, 331–334.
- Harrison A. and Thode H. (1958) Mechanism of the bacterial reduction of sulphate from isotope fractionation studies. *Trans. Faraday Soc.* **54**, 84–92.
- Harrison B. K., Zhang H., Berelson W. and Orphan V. J. (2009) Variations in archaeal and bacterial diversity associated with the sulfate-methane transition zone in continental margin sediments (Santa Barbara Basin, California). *Appl. Environ. Microbiol.* **75**, 1487–1499.
- Herlihy A. T. and Mills A. L. (1985) Sulfate reduction in freshwater sediments receiving acid mine drainage. *Appl. Environ. Microbiol.* **49**, 179–186.
- Herrmann A. M., Ritz K., Nunan N., Clode P. L., Pett-Ridge J., Kilburn M. R., Murphy D. V., O'Donnell A. G. and Stockdale E. A. (2007) Nano-scale secondary ion mass spectrometry – a new analytical tool in biogeochemistry and soil ecology: A review article. *Soil Biol. Biochem.* **39**, 1835–1850.
- Hinrichs K. U. and Boetius A. (2003) *The Anaerobic Oxidation of Methane: New Insights in Microbial Ecology and Biogeochemistry*. Springer, Berlin Heidelberg, pp. 457–477.
- Hoek J. and Canfield D. E. (2008) Controls on isotope fractionation during dissimilatory sulfate reduction. In *Microbial Sulfur Metabolism* (eds. C. Dahl and C. Friedrich). Springer, Berlin Heidelberg, pp. 273–284.
- Holmer M. and Storkholm P. (2001) Sulphate reduction and sulphur cycling in lake sediments: a review. *Freshw. Biol.* **46**, 431–451.
- Holmkvist L., Ferdelman T. G. and Jorgensen B. B. (2011) A cryptic sulfur cycle driven by iron in the methane zone of marine sediment (Aarhus Bay, Denmark). *Geochim. Cosmochim. Acta* **75**, 3581–3599.
- Hordijk K. A., Hagenaars C. P. M. M. and Cappenberg T. E. (1985) Kinetic studies of bacterial sulfate reduction in freshwater sediments by high-pressure liquid chromatography and microdistillation. *Appl. Environ. Microbiol.* **49**, 434–440.
- Hren M. T., Tice M. M. and Chamberlain C. P. (2009) Oxygen and hydrogen isotope evidence for a temperate climate 3.42 billion years ago. *Nature* **462**, 205–208.
- Ingvorsen K. and Jrgensen B. (1984) Kinetics of sulfate uptake by freshwater and marine species of *Desulfobrevibrio*. *Arch. Microbiol.* **139**, 61–66.
- Ingvorsen K., Zehnder A. J. B. and Jrgensen B. B. (1984) Kinetics of sulfate and acetate uptake by *Desulfobacter postgatei*. *Appl. Environ. Microbiol.* **47**, 403–408.
- Iversen N. and Jrgensen B. B. (1993) Diffusion coefficients of sulfate and methane in marine sediments: influence of porosity. *Geochim. Cosmochim. Acta* **57**, 571–578.
- Johnston D. T., Farquhar J. and Canfield D. E. (2007) Sulfur isotope insights into microbial sulfate reduction: when microbes meet models. *Geochim. Cosmochim. Acta* **71**, 3929–3947.

- Jørgensen B. B. (1977) Bacterial sulfate reduction within reduced microniches of oxidized marine sediments. *Mar. Biol.* **41**, 7–17.
- Jørgensen B. B. (1979) A theoretical model of the stable sulfur isotope distribution in marine sediments. *Geochim. Cosmochim. Acta* **43**, 363–374.
- Kaplan I. and Rittenberg S. (1964) Microbiological fractionation of sulphur isotopes. *J. Gen. Microbiol.* **34**, 195–212.
- Karp-Boss L., Boss E. and Jumars P. (1996) Nutrient fluxes to planktonic osmotrophs in the presence of fluid motion. *Oceanogr. Mar. Biol.* **34**, 71–108.
- Kertesz M. A. (2001) Bacterial transporters for sulfate and organosulfur compounds. *Res. Microbiol.* **152**, 279–290.
- Kirboe T. and Jackson G. A. (2001) Marine snow, organic solute plumes, and optimal chemosensory behavior of bacteria. *Limnol. Oceanogr.* **46**, 1309–1318.
- Knauth L. P. (2005) Temperature and salinity history of the Precambrian ocean: implications for the course of microbial evolution. *Palaeogeogr. Palaeoclimatol. Palaeoecol.* **219**, 53–69.
- Knoblauch C., Jørgensen B. B. and Harder J. (1999) Community size and metabolic rates of psychrophilic sulfate-reducing bacteria in arctic marine sediments. *Appl. Environ. Microbiol.* **65**, 4230–4233.
- Koch A. L. (1990) Diffusion the crucial process in many aspects of the biology of bacteria. In *Advances in Microbial Ecology*. Springer, pp. 37–70.
- Koch A. L. (1996) What size should a bacterium be? A question of scale. *Annu. Rev. Microbiol.* **50**, 317–348.
- Konwar K. M., Hanson N. W., Pagé A. P. and Hallam S. J. (2013) Metapathways: a modular pipeline for constructing pathway/genome databases from environmental sequence information. *BMC Bioinformatics* **14**, 202.
- Kowalewski M. and Bambach R. K. (2008) The limits of paleontological resolution. In *High Resolution Approaches in Stratigraphic Paleontology* (ed. P. J. Harries), pp. 1–48. Topics in Geobiology. Springer, Netherlands.
- Kuivila K., Murray J., Devol A. and Novelli P. (1989) Methane production, sulfate reduction and competition for substrates in the sediments of Lake Washington. *Geochim. Cosmochim. Acta* **53**, 409–416.
- Lambert I. B., Donnelly T. H., Dunlop J. S. R. and Groves D. I. (1978) Stable isotopic compositions of early Archaean sulphate deposits of probable evaporitic and volcanogenic origins. *Nature* **276**, 808–811.
- Leavitt W. D., Haley I., Bradley A. S. and Johnston D. T. (2013) Influence of sulfate reduction rates on the Phanerozoic sulfur isotope record. *Proc. Natl. Acad. Sci. U.S.A.* **110**, 11244–11249.
- Leloup J., Fossing H., Kohls K., Holmkvist L., Borowski C. and Jørgensen B. B. (2009) Sulfate-reducing bacteria in marine sediment (Aarhus Bay, Denmark): abundance and diversity related to geochemical zonation. *Environ. Microbiol.* **11**, 1278–1291.
- Lever M. A., Rogers K. L., Lloyd K. G., Overmann J., Schink B., Thauer R. K., Hoehler T. M. and Jørgensen B. B. (2015) Life under extreme energy limitation: a synthesis of laboratory- and field-based investigations. *FEMS Microbiol. Rev.* **39**, 688–728.
- Lewis A. E. (2010) Review of metal sulphide precipitation. *Hydrometallurgy* **104**, 222–234.
- Llobet-Brossa E., Rabus R., Böttcher M. E., Könneke M., Finke N., Schramm A., Meyer R. L., Gröttschel S., Rosselló-Mora R. and Amann R. (2002) Community structure and activity of sulfate-reducing bacteria in an intertidal surface sediment: a multi-method approach. *Aquat. Microb. Ecol.* **29**, 211–226.
- Lovley D. R. and Klug M. J. (1983) Sulfate reducers can outcompete methanogens at freshwater sulfate concentrations. *Appl. Environ. Microbiol.* **45**, 187–192.
- Lovley D. R. and Klug M. J. (1986) Model for the distribution of sulfate reduction and methanogenesis in freshwater sediments. *Geochim. Cosmochim. Acta* **50**, 11–18.
- Luepke J. J. and Lyons T. W. (2001) Pre-Rodinian (Mesoproterozoic) supercontinental rifting along the western margin of Laurentia: geochemical evidence from the Belt-Purcell Supergroup. *Precamb. Res.* **111**, 79–90.
- Lyons T. W. (1997) Sulfur isotopic trends and pathways of iron sulfide formation in upper holocene sediments of the anoxic black sea. *Geochim. Cosmochim. Acta* **61**, 3367–3382.
- Lyons T. W., Luepke J. J., Schreiber M. E. and Zieg G. A. (2000) Sulfur geochemical constraints on Mesoproterozoic restricted marine deposition: lower Belt Supergroup, northwestern United States. *Geochim. Cosmochim. Acta* **64**, 427–437.
- Ma S., Noble A., Butcher D., Trouwborst R. E. and Luther, III, G. W. (2006) Removal of H₂S via an iron catalytic cycle and iron sulfide precipitation in the water column of dead end tributaries. *Estuar. Coast. Shelf Sci.* **70**, 461–472.
- Machel H. G., Krouse H. R. and Sassen R. (1995) Products and distinguishing criteria of bacterial and thermochemical sulfate reduction. *Appl. Geochem.* **10**, 373–389.
- Magariyama Y., Sugiyama S., Muramoto K., Kawagishi I., Imae Y. and Kudo S. (1995) Simultaneous measurement of bacterial flagellar rotation rate and swimming speed. *Biophys. J.* **69**, 2154–2162.
- Mitchell J. G. and Barbara G. M. (1999) High speed marine bacteria use sodium-ion and proton driven motors. *Aquat. Microb. Ecol.* **18**, 227–233.
- Mitchell J. G., Pearson L., Bonazinga A., Dillon S., Khouri H. and Paxinos R. (1995a) Long lag times and high velocities in the motility of natural assemblages of marine bacteria. *Appl. Environ. Microbiol.* **61**, 877–882.
- Mitchell J. G., Pearson L., Dillon S. and Kantalis K. (1995b) Natural assemblages of marine bacteria exhibiting high-speed motility and large accelerations. *Appl. Environ. Microbiol.* **61**, 4436–4440.
- Monod J. (1942) *Recherches sur la croissance des cultures bactériennes*. Hermann & cie, Paris.
- Nauhaus K., Albrecht M., Elvert M., Boetius A. and Widdel F. (2007) In vitro cell growth of marine archaeal–bacterial consortia during anaerobic oxidation of methane with sulfate. *Environ. Microbiol.* **9**, 187–196.
- Nishina T., Ura H. and Uchida I. (1997) Determination of chemical diffusion coefficients in metal hydride particles with a microelectrode technique. *J. Electrochem. Soc.* **144**, 1273–1277.
- Ohmoto H. and Rye R. (1979) Isotopes of sulfur and carbon. In *Geochemistry of Hydrothermal Ore Deposits* (ed. H. L. Barnes). Wiley, New York, pp. 509–567.
- Orphan V. J., Hinrichs K. U., Ussler W., Paull C. K., Taylor L. T., Sylva S. P., Hayes J. M. and Delong E. F. (2001) Comparative analysis of methane-oxidizing archaea and sulfate-reducing bacteria in anoxic marine sediments. *Appl. Environ. Microbiol.* **67**, 1922–1934.
- Otake T., Lasaga A. C. and Ohmoto H. (2008) Ab initio calculations for equilibrium fractionations in multiple sulfur isotope systems. *Chem. Geol.* **249**, 357–376.
- Pallud C. and Van Cappellen P. (2006) Kinetics of microbial sulfate reduction in estuarine sediments. *Geochim. Cosmochim. Acta* **70**, 1148–1162.
- Pasciak W. J. and Gavis J. (1974) Transport limitation of nutrient uptake in phytoplankton. *Limnol. Oceanogr.* **19**, 881–888.
- Paytan A., Kastner M., Campbell D. and Thiemens M. H. (1998) Sulfur isotopic composition of Cenozoic seawater sulfate. *Science* **282**, 1459–1462.

- Price F. T. and Shieh Y. (1979) Fractionation of sulfur isotopes during laboratory synthesis of pyrite at low temperatures. *Chem. Geol.* **27**, 245–253.
- Pruesse E., Quast C., Knittel K., Fuchs B. M., Ludwig W., Peplis J. and Glöckner F. O. (2007) SILVA: a comprehensive online resource for quality checked and aligned ribosomal RNA sequence data compatible with ARB; a comprehensive online resource for quality checked and aligned ribosomal RNA sequence data compatible with ARB. *Nucleic Acids Res.* **35**, 7188–7196.
- Purcell E. M. (1977) Life at low Reynolds number. *Am. J. Phys.* **45**, 3–11.
- Raven M. R., Sessions A. L., Fischer W. W. and Adkins J. F. (2016) Sedimentary pyrite $\delta^{34}\text{S}$ differs from porewater sulfide in Santa Barbara basin: proposed role of organic sulfur. *Geochim. Cosmochim. Acta* **186**, 120–134.
- Ravenschlag K., Sahm K., Knoblauch C., Jørgensen B. B. and Amann R. (2000) Community structure, cellular rRNA content, and activity of sulfate-reducing bacteria in marine arctic sediments. *Appl. Environ. Microbiol.* **66**, 3592–3602.
- Rees C. (1973) A steady-state model for sulphur isotope fractionation in bacterial reduction processes. *Geochim. Cosmochim. Acta* **37**, 1141–1162.
- Revsbech N. P. and Jørgensen B. B. (1986) Microelectrodes: their use in microbial ecology. In *Advances in Microbial Ecology*. Springer, pp. 293–352.
- Richter F. M., Mendybaev R. A., Christensen J. N., Hutcheon I. D., Williams R. W., Sturchio N. C. and Beloso, Jr., A. D. (2006) Kinetic isotopic fractionation during diffusion of ionic species in water. *Geochim. Cosmochim. Acta* **70**, 277–289.
- Rickard D. (1997) Kinetics of pyrite formation by the H_2S oxidation of iron (II) monosulfide in aqueous solutions between 25 and 125 °C: the rate equation. *Geochim. Cosmochim. Acta* **61**, 115–134.
- Rickard D. and Luther G. W. (1997) Kinetics of pyrite formation by the H_2S oxidation of iron (II) monosulfide in aqueous solutions between 25 and 125 °C: The mechanism. *Geochim. Cosmochim. Acta* **61**, 135–147.
- Robert F. and Chaussidon M. (2006) A palaeotemperature curve for the Precambrian oceans based on silicon isotopes in cherts. *Nature* **443**, 969–972.
- Savarino J., Romero A., Cole-Dai J., Bekki S. and Thiemens M. H. (2003) UV induced mass-independent sulfur isotope fractionation in stratospheric volcanic sulfate. *Geophys. Res. Lett.* **30**, 2131.
- Sharqawy M. H., Lienhard J. H. and Zubair S. M. (2010) Thermophysical properties of seawater: a review of existing correlations and data. *Desal. Water Treat.* **16**, 354–380.
- Shaw A., Takacs I., Pagilla K., Riffat R., DeClippel H., Wilson C. and Murthy S. (2015) Toward universal half-saturation coefficients: describing extant K_s as a function of diffusion. *Water Environ. Res.* **87**, 387–391.
- Shen Y., Buick R. and Canfield D. E. (2001) Isotopic evidence for microbial sulphate reduction in the early Archaean era. *Nature* **410**, 77–81.
- Sim M. S., Bosak T. and Ono S. (2011a) Large sulfur isotope fractionation does not require disproportionation. *Science* **333**, 74–77.
- Sim M. S., Ono S., Donovan K., Templer S. P. and Bosak T. (2011b) Effect of electron donors on the fractionation of sulfur isotopes by a marine *Desulfovibrio* sp. *Geochim. Cosmochim. Acta* **75**, 4244–4259.
- Sim M. S., Ono S. and Bosak T. (2012) Effects of iron and nitrogen limitation on sulfur isotope fractionation during microbial sulfate reduction. *Appl. Environ. Microbiol.* **78**, 8368–8376.
- Sleep N. H. (2010) The hadean–archaean environment. *Cold Spring Harbor Perspect. Biol.* **2**.
- Smith S. L., Yamanaka Y., Pahlow M. and Oschlies A. (2009) Optimal uptake kinetics: physiological acclimation explains the pattern of nitrate uptake by phytoplankton in the ocean. *Mar. Ecol. Prog. Ser.* **384**, 1–12.
- Sonne-Hansen J., Westermann P. and Ahring B. K. (1999) Kinetics of sulfate and hydrogen uptake by the thermophilic sulfate-reducing bacteria *Thermodesulfobacterium* sp. strain jsp and *Thermodesulfovibrio* sp. strain r1ha3. *Appl. Environ. Microbiol.* **65**, 1304–1307.
- Stewart P. S. (2003) Diffusion in biofilms. *J. Bacteriol.* **185**, 1485–1491.
- Stocker R. (2012) Marine microbes see a sea of gradients. *Science* **338**, 628–633.
- Strauss H. (1997) The isotopic composition of sedimentary sulfur through time. *Palaeogeogr. Palaeoclimatol. Palaeoecol.* **132**, 97–118.
- Suits N. S. and Wilkin R. T. (1998) Pyrite formation in the water column and sediments of a meromictic lake. *Geology* **26**, 1099–1102.
- Tarpgaard I. H., Ry H. and Jørgensen B. B. (2011) Concurrent low- and high-affinity sulfate reduction kinetics in marine sediment. *Geochim. Cosmochim. Acta* **75**, 2997–3010.
- Thullner M., Kampara M., Richnow H. H., Harms H. and Wick L. Y. (2008) Impact of bioavailability restrictions on microbially induced stable isotope fractionation. 1. theoretical calculation. *Environ. Sci. Technol.* **42**, 6544–6551.
- Tomlinson T. and Snaddon D. (1966) Biological oxidation of sewage by films of microorganisms. *Air Water Pollut.* **10**, 865.
- Treude T., Krause S., Maltby J., Dale A. W., Coffin R. and Hamdan L. J. (2014) Sulfate reduction and methane oxidation activity below the sulfate-methane transition zone in Alaskan Beaufort Sea continental margin sediments: Implications for deep sulfur cycling. *Geochim. Cosmochim. Acta* **144**, 217–237.
- Ueno Y., Ono S., Rumble D. and Maruyama S. (2008) Quadruple sulfur isotope analysis of ca. 3.5 Ga Dresser Formation: new evidence for microbial sulfate reduction in the early Archaean. *Geochim. Cosmochim. Acta* **72**, 5675–5691.
- Wacey D., McLoughlin N., Whitehouse M. J. and Kilburn M. R. (2010) Two coexisting sulfur metabolisms in a ca. 3400 Ma sandstone. *Geology* **38**, 1115–1118.
- Webster G., Sass H., Cragg B. A., Gorra R., Knab N. J., Green C. J., Mathes F., Fry J. C., Weightman A. J. and Parkes R. J. (2011) Enrichment and cultivation of prokaryotes associated with the sulphate–methane transition zone of diffusion-controlled sediments of Aarhus Bay, Denmark, under heterotrophic conditions. *FEMS Microbiol. Ecol.* **77**, 248–263.
- Widdel F. and Bak F. (1992) Gram-negative mesophilic sulfate-reducing bacteria. In *The Prokaryotes* (eds. A. Balows, H. Trüper, M. Dworkin, W. Harder and K. H. Schleifer). Springer, New York, pp. 3352–3378.
- Wing B. A. and Halevy I. (2014) Intracellular metabolite levels shape sulfur isotope fractionation during microbial sulfate respiration. *Proc. Natl. Acad. Sci. U.S.A.*
- Wortmann U. G. and Chernyavsky B. M. (2011) The significance of isotope specific diffusion coefficients for reaction-transport models of sulfate reduction in marine sediments. *Geochim. Cosmochim. Acta* **75**, 3046–3056.
- Zhilina T. N., Zavarzin G. A., Rainey F. A., Pikuta E. N., Osipov G. A. and Kostrikin N. A. (1997) *Desulfonatovibrio hydrogenovorans* gen. nov., sp. nov., an alkaliphilic, sulfate-reducing bacterium. *Int. J. Syst. Evol. Microbiol.* **47**, 144–149.

Microscale reservoir effects on microbial sulfur isotope
fractionation
- Supplementary Material -

Stilianos Louca, Sean A. Crowe

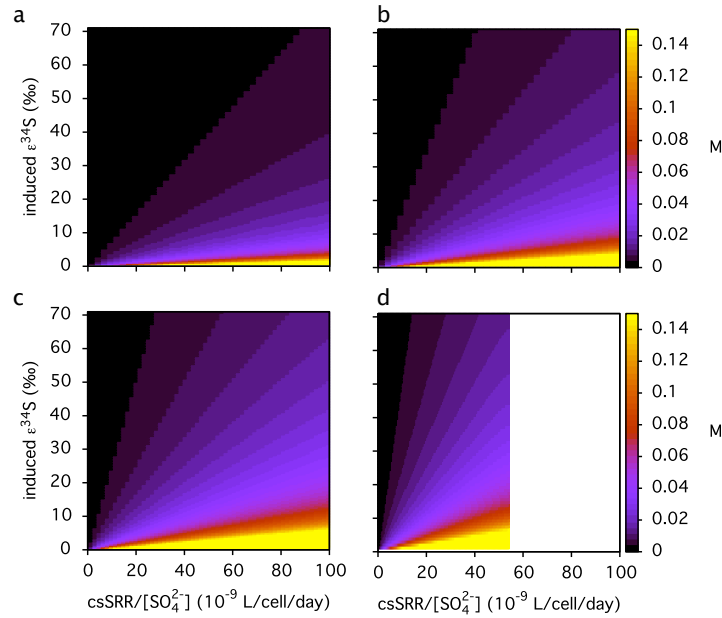


Figure S1: Values of the auxiliary variable M for varying induced fractionation factors (vertical axis) and relative cell-specific sulfate reduction rates ($\text{csSRR}/[\text{SO}_4^{2-}]$), horizontal axis). Parameters are a typical diffusion coefficient for seawater ($D_{32} = 5.8 \times 10^{-10} \text{ m}^2/\text{s}$, top row) and marine sediments ($D_{32} = 2 \times 10^{-10} \text{ m}^2/\text{s}$, bottom row) (Iversen and Jørgensen, 1993), and a large (left column) and small (right column) cell radius ($R = 0.25 - 0.5 \mu\text{m}$; Widdel and Bak, 1992). The white region in (d) corresponds to unrealistically high csSRR, i.e. which exceed the rate sustainable by extracellular diffusive transport.

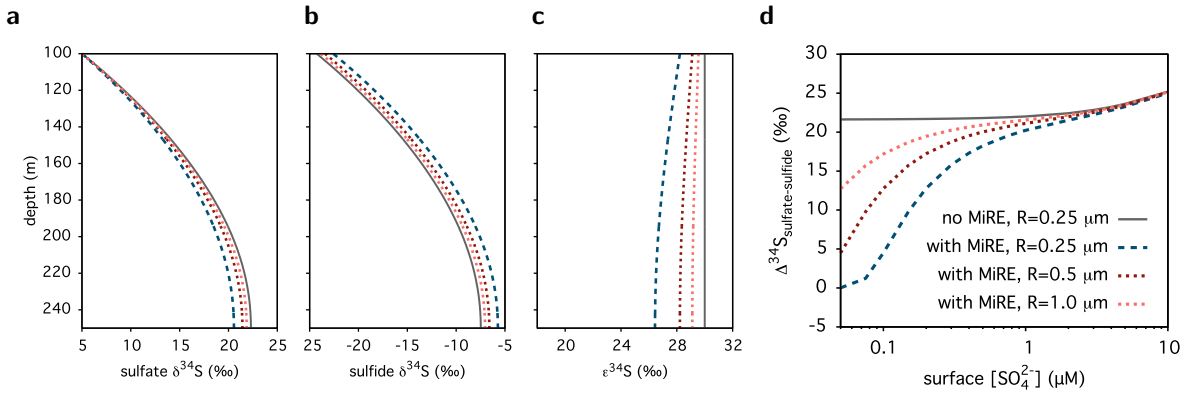


Figure S2: Sensitivity of the Archean ocean model (Section 2.5 in the main article) with respect to varying MSR cell radii. (a) Sulfate S isotope composition, (b) exported sulfide S isotopologue composition and (c) expressed S isotope fractionation (w.r.t. background sulfate isotopologue composition) at various depths, for a fixed “surface” sulfate concentration ($S_t = 1 \mu\text{M}$). (d) Mean fractionation expressed in deposited pyrites with respect to the surface sulfate pool, for various surface sulfate concentrations. Continuous and dashed/dotted curves show model predictions without and with microscale reservoir effects (MiRE), respectively. Blue dashed curves correspond to the cell radius used in the main article ($R = 0.25 \mu\text{m}$). Red dotted curves correspond to alternative cell radii (dark red $R = 0.5 \mu\text{m}$, light red $R = 1.0 \mu\text{m}$; Widdel and Bak, 1992; Nauhaus *et al.*, 2007). All other model parameters are as in Fig. 5 in the main article. Note that the cell radius does not affect model predictions when MiREs are ignored.

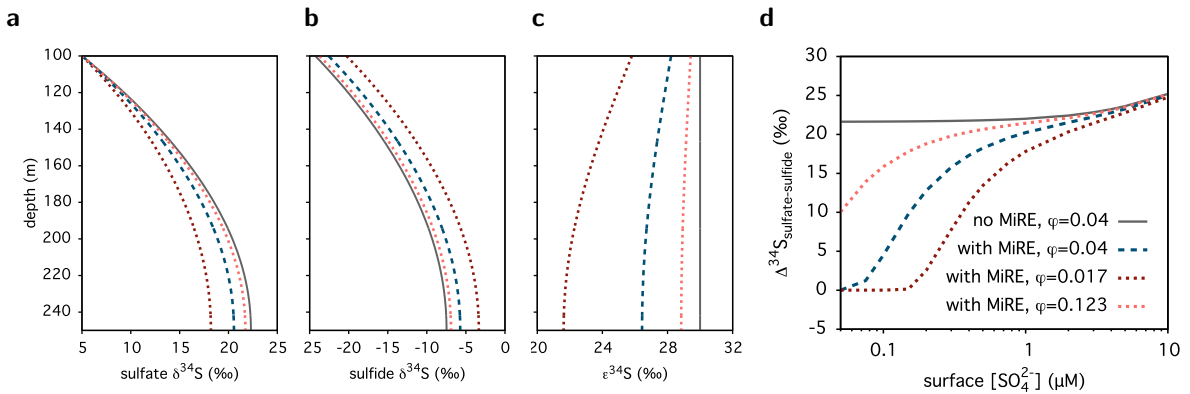


Figure S3: Sensitivity of the Archean ocean model (Section 2.5 in the main article) with respect to varying fractions of active MSR cells (FAC). (a) Sulfate S isotope composition, (b) exported sulfide S isotopologue composition and (c) expressed S isotope fractionation (w.r.t. background sulfate isotopologue composition) at various depths, for a fixed “surface” sulfate concentration ($S_t = 1 \mu\text{M}$). (d) Mean fractionation expressed in deposited pyrites with respect to the surface sulfate pool, for various surface sulfate concentrations. Continuous and dashed/dotted curves show model predictions without and with microscale reservoir effects (MiRE), respectively. Blue dashed curves correspond to the FAC used in the main article ($\varphi = 0.04$; Haglund *et al.*, 2002). Red dotted curves correspond to alternative FACs (dark red $\varphi = 0.017$, light red $\varphi = 0.123$; Llobet-Brossa *et al.*, 2002). All other model parameters are as in Fig. 5 in the main article. Note that the FAC does not affect model predictions when MiREs are ignored.

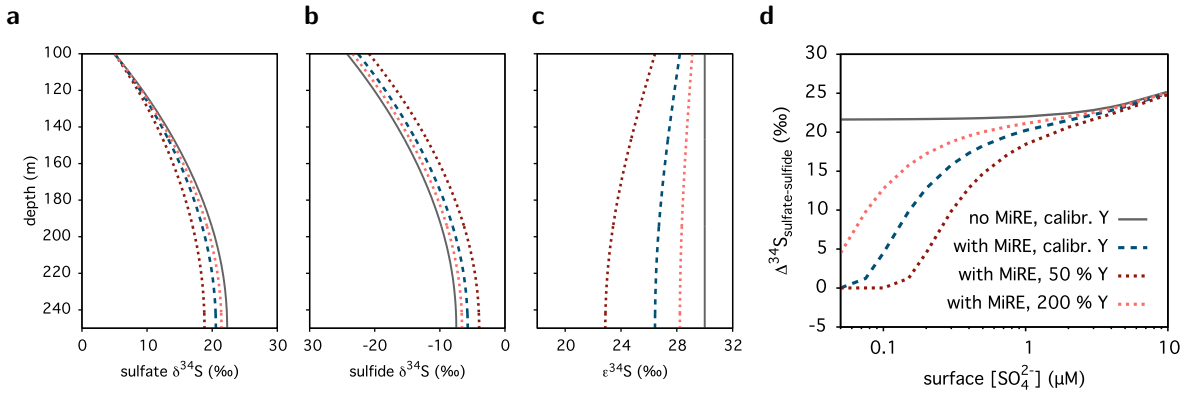


Figure S4: Sensitivity of the Archean ocean model (Section 2.5 in the main article), with respect to the calibrated proportionality factor Y (Eq. 40 in the main article). (a) Sulfate S isotope composition, (b) exported sulfide S isotopologue composition and (c) expressed S isotope fractionation (w.r.t. background sulfate isotopologue composition) at various depths, for a fixed “surface” sulfate concentration ($S_t = 1 \mu\text{M}$). (d) Mean fractionation expressed in deposited pyrites with respect to the surface sulfate pool, for various surface sulfate concentrations. Continuous and dashed/dotted curves show model predictions without and with microscale reservoir effects (MiRE), respectively. Blue dashed curves correspond to the calibrated proportionality factor used in the main article ($Y = 1.022 \times 10^{15}$ (cells \times days)/mol). Red dotted curves correspond to alternative factors (dark red $Y = 50\%$ of the calibrated value, light red $Y = 200\%$ of the calibrated value). All other model parameters are as in Fig. 5 in the main article. Note that the factor Y does not affect model predictions when MiREs are ignored.

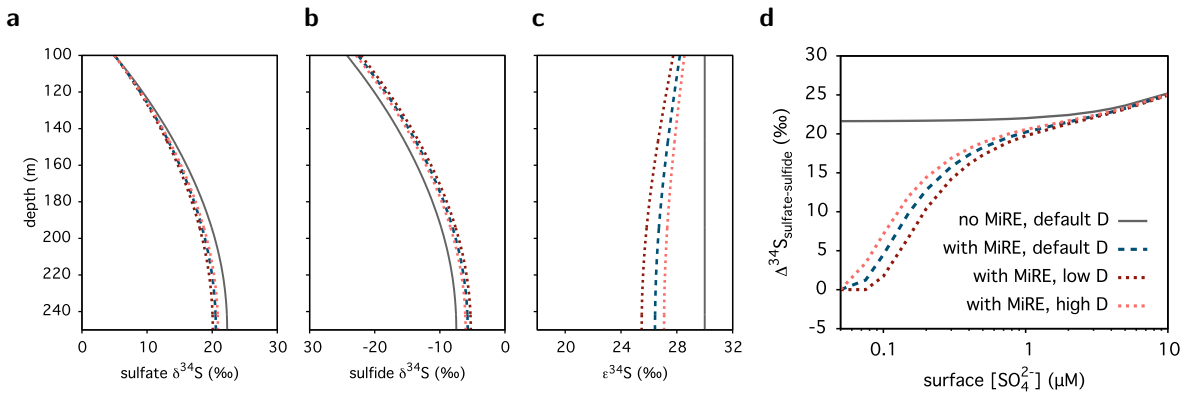


Figure S5: Sensitivity of the Archean ocean model (Section 2.5 in the main article) with respect to varying sulfate diffusivities. (a) Sulfate S isotope composition, (b) exported sulfide S isotopologue composition and (c) expressed S isotope fractionation (w.r.t. background sulfate isotopologue composition) at various depths, for a fixed “surface” sulfate concentration ($S_t = 1 \mu\text{M}$). (d) Mean fractionation expressed in deposited pyrites with respect to the surface sulfate pool, for various surface sulfate concentrations. Continuous and dashed/dotted curves show model predictions without and with microscale reservoir effects (MiRE), respectively. Blue dashed curves correspond to the sulfate diffusion coefficient used in the main article ($D = 15.2 \times 10^{-10} \text{ m}^2/\text{s}$). Red dotted curves correspond to alternative diffusion coefficients, based on alternative temperature (T) and salinity (S) scenarios (dark red $D = 12.0 \times 10^{-10} \text{ m}^2/\text{s}$ based on $T = 40^\circ\text{C}$ and $S = 70\%$, light red $D = 18.6 \times 10^{-10} \text{ m}^2/\text{s}$ based on $T = 70^\circ\text{C}$ and $S = 50\%$; Boudreau, 1997; Robert and Chaussidon, 2006). All other model parameters are as in Fig. 5 in the main article. Note that the sulfate diffusivity does not affect model predictions when MiREs are ignored.

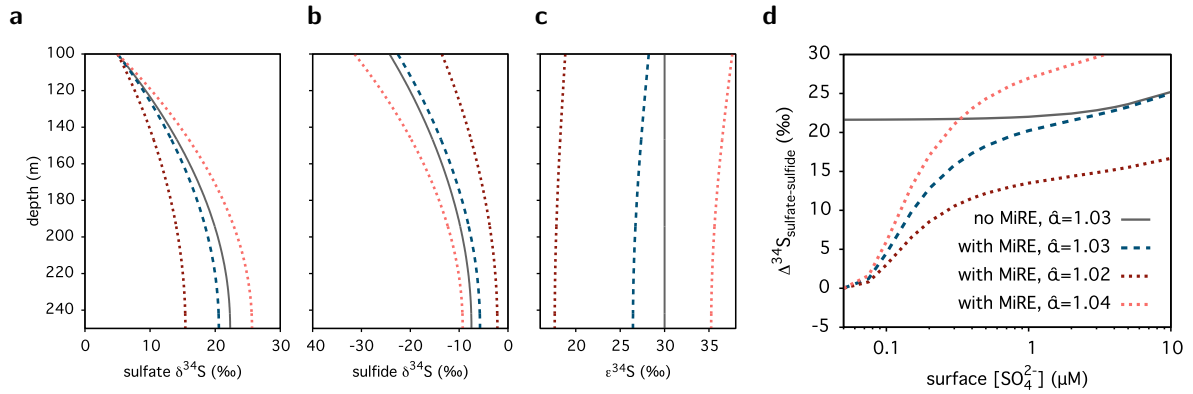


Figure S6: Sensitivity of the Archean ocean model (Section 2.5 in the main article) with respect to induced fractionation factor $\bar{\alpha}$. (a) Sulfate S isotope composition, (b) exported sulfide S isotopologue composition and (c) expressed S isotope fractionation (w.r.t. background sulfate isotopologue composition) at various depths, for a fixed “surface” sulfate concentration ($S_t = 1 \mu\text{M}$). (d) Mean fractionation expressed in deposited pyrites with respect to the surface sulfate pool, for various surface sulfate concentrations. Continuous and dashed/dotted curves show model predictions without and with microscale reservoir effects (MiRE), respectively. Blue dashed curves and grey continuous curves correspond to the fractionation factor used in the main article ($\bar{\alpha} = 1.03$). Red dotted curves correspond to alternative fractionation factors (dark red $\bar{\alpha} = 1.02$, light red $\bar{\alpha} = 1.04$). All other model parameters are as in Fig. 5 in the main article.

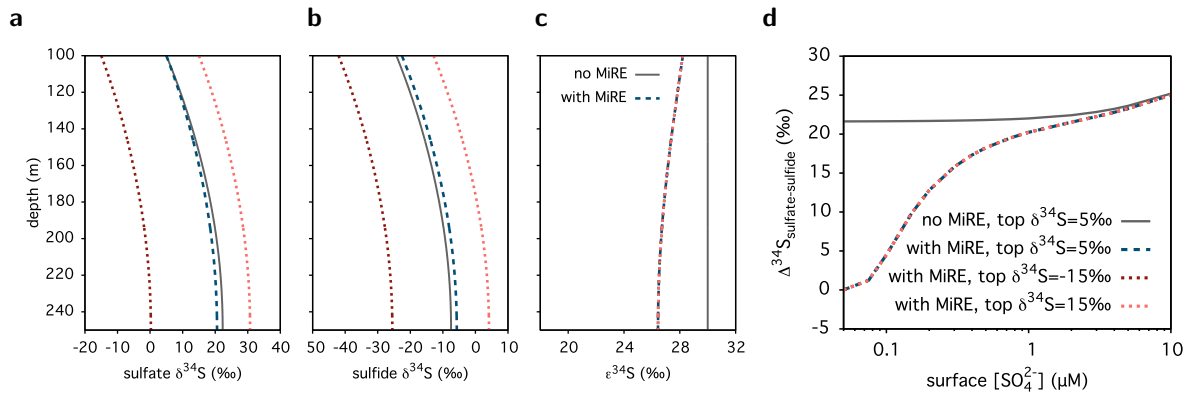


Figure S7: Sensitivity of the Archean ocean model (Section 2.5 in the main article) with respect to varying sulfate $\delta^{34}\text{S}$ at the top (“surface”). (a) Sulfate S isotope composition, (b) exported sulfide S isotopologue composition and (c) expressed S isotope fractionation (w.r.t. background sulfate isotopologue composition) at various depths, for a fixed surface sulfate concentration ($S_t = 1 \mu\text{M}$). (d) Mean fractionation expressed in deposited pyrites with respect to the surface sulfate pool, for various surface sulfate concentrations. Continuous and dashed/dotted curves show model predictions without and with microscale reservoir effects (MiRE), respectively. Blue dashed curves and grey continuous curves correspond to the surface sulfate $\delta^{34}\text{S}$ used in the main article ($\delta^{34}\text{S} = 5\text{‰}$, w.r.t. Canyon Diablo Troilite; Ueno *et al.*, 2008), while red dotted curves correspond to alternative surface sulfate $\delta^{34}\text{S}$ (dark red $\delta^{34}\text{S} = -15\text{‰}$, light red $\delta^{34}\text{S} = 15\text{‰}$; Lambert *et al.*, 1978; Shen *et al.*, 2001). All other model parameters are as in Fig. 5 in the main article.

Table S1: Maximum bulk sulfate reduction rates (V_{\max}) at various depths, as used in the Archean ocean model (Section 2.5 in the main article). Values at the specified depths are estimated based on modern respiration kinetics in anoxic ocean water columns (Crowe *et al.*, 2014, Table S2 therein). At intermediate depths V_{\max} was interpolated using splines.

depth (m)	V_{\max} ($\mu\text{M}/\text{year}$)
100	0.864
150	0.404
200	0.236
250	0.156

Table S2: Taxa identified as sulfate respirers in the Lake Matano metagenomes, based on previous literature. Details in section 2.5 of the main article.

taxon	reference
<i>Ammonifex degensii</i>	Huber <i>et al.</i> , 1996
<i>Desulfovibrio alaskensis</i>	Keller <i>et al.</i> , 2014
<i>Desulfotalea</i> spp.	Garrity, 2005
Desulfobacterales	Garrity, 2005
<i>Desulfovibrio</i> spp.	Garrity, 2005
<i>Desulfotomaculum</i> spp.	Vos <i>et al.</i> , 2011
<i>Desulfosporosinus</i> spp.	Vos <i>et al.</i> , 2011
Desulfohalobiaceae	Garrity, 2005
<i>Desulfomonile</i> spp.	Garrity, 2005

S1 Correcting calibration curves

In this section we show how calibration curves for S-isotope fractionation, obtained experimentally in well-mixed reactors (Habicht *et al.*, 2002; Wing and Halevy, 2014), can be corrected to account for the microscale reservoir effect in diffusion-limited environments. Specifically, we assume that the induced (i.e. true) fractionation $\tilde{\alpha}$ is a known function of the cell-specific sulfate reduction rate (csSRR) J , the near-cell sulfate concentration \tilde{S} and potentially the near-cell sulfide concentration \tilde{X} :

$$\tilde{\alpha} = \tilde{A}(J, \tilde{S}, \tilde{X}). \quad (1)$$

The function \tilde{A} will typically be in the form of a regression or interpolation curve, fitted to measured fractionation data. Given the above information, we show how one can infer the apparent fractionation α as a function of the background sulfate concentration S , the background sulfide concentration X (if applicable), the csSRR J , the cell radius R , the background sulfate isotopic composition ($r = [^{34}\text{SO}_4^{2-}]/[^{32}\text{SO}_4^{2-}]$), as well as the diffusion coefficients D_{32} , D_{34} , E_{32} and E_{34} of $^{32}\text{SO}_4^{2-}$, $^{34}\text{SO}_4^{2-}$, H_2S^{32} and H_2S^{34} , respectively.

Recall that

$$\alpha = F(J/S, R, r, D_{32}, D_{34}, \tilde{\alpha}), \quad (2)$$

where F is a known explicit function derived in Eq. (13) in the main article. The near-cell concentrations \tilde{S} and \tilde{X} can be obtained from S and X :

$$\tilde{S} = \tilde{s}(J, S, R, r, D_{32}, D_{34}, \alpha), \quad \tilde{X} = \tilde{x}(J, X, R, r, E_{32}, E_{34}, \alpha), \quad (3)$$

where the functions \tilde{s} and \tilde{x} are given by

$$\begin{aligned} \tilde{s} &= S - \frac{J}{4\pi R D_{32}} \left[1 + \frac{r}{\alpha + r} \left(\frac{D_{32}}{D_{34}} - 1 \right) \right], \\ \tilde{x} &= X + \frac{J}{4\pi R E_{32}} \left[1 + \frac{r}{\alpha + r} \left(\frac{E_{32}}{E_{34}} - 1 \right) \right]. \end{aligned} \quad (4)$$

The above formula for \tilde{s} can be obtained by combining Eq. (3) with equations (8) and (9) in the main article. The formula for \tilde{x} is obtained in a similar way. Combining equations (1), (2) and (3) yields

$$\alpha = F \left[J/S, R, r, D_{32}, D_{34}, \tilde{A}(J, \tilde{s}(J, S, R, r, D_{32}, D_{34}, \alpha), \tilde{x}(J, X, R, r, E_{32}, E_{34}, \alpha)) \right]. \quad (5)$$

Solving Eq. (5) for α gives α implicitly as a function of J , S , X , R , r , D_{32} , D_{34} , E_{32} and E_{34} . In general, depending on the structure of \tilde{A} , this will only be possible numerically or graphically.

In practice, diffusion-driven fractionation is low ($D_{32}/D_{34} \approx 1$; Richter *et al.*, 2006) and $r \ll \alpha$, so that Eq. (4) can be approximated as

$$\tilde{s} \approx S - \frac{J}{4\pi R D_{32}}, \quad \tilde{x} \approx X + \frac{J}{4\pi R E_{32}}. \quad (6)$$

The error of these approximations is small when compared to the background sulfate and sulfide levels. When $D_{32} = D_{34}$ and $E_{32} = E_{34}$, Eq. (6) becomes exact. With these approximations, Eq. (5) becomes an explicit formula for α ,

$$\alpha \approx F \left[J/S, R, r, D_{32}, D_{34}, \tilde{A} \left(J, S - \frac{J}{4\pi R D_{32}}, X + \frac{J}{4\pi R E_{32}} \right) \right], \quad (7)$$

where F is given by Eq. (13) in the main article. From (7) it becomes apparent that in general at least two processes alter α , when compared to the case of unlimited diffusion: (a) The formation of a sulfate (sulfide) gradient leads to near-cell sulfate (sulfide) levels that differ from background concentrations. Hence, if the true fractionation depends on sulfate (sulfide) concentrations, these differences will lead to an altered true fractionation (Wing and Halevy, 2014). (b) The microscale reservoir effect leads to a difference between the true and the apparent fractionation. This effect would be present even if the true fractionation was constant.

S2 Cylindrical cells

In the following we modify the model derivation of the main article (section 2.2.2) for narrow cylindrical (“rod-shaped”) cells to examine the robustness of our results with respect to non-spherical shapes. For simplicity, we shall assume that sulfate fluxes are evenly distributed across the cell surface and that cells are very narrow (compared to their length). Hence, the extracellular sulfate distribution is approximately the same as if the cell was a thin line segment, consuming sulfate at a constant length-specific rate (e.g. mol sulfate consumed per μm per day). Hence, at steady state the sulfate profiles $U_{32} = [{}^3\text{SO}_4^{2-}]$ and $U_{34} = [{}^3\text{SO}_4^{2-}]$ approximately satisfy the Laplace equation in cylindrical coordinates:

$$\frac{D_i}{\rho} \frac{\partial}{\partial \rho} \left(\rho \frac{\partial U_i}{\partial \rho} \right) + D_i \frac{\partial^2 U_i}{\partial z^2} - \frac{J_i}{L} \delta(\rho) \Theta(|z| - L/2) = 0, \quad (8)$$

where i stands for either “32” or “34”, J_i is the cell-specific consumption rate (sulfate consumed per cell per time), $\delta(\rho)$ is the Dirac distribution in the 2D plane in polar coordinates, Θ is the Heaviside function and L is the cylinder length. The z -axis is aligned to the cylinder’s symmetry axis. In addition, U_i satisfies the boundary condition

$$U_i|_{\infty} = S_i, \quad (9)$$

where S_i is the background concentration. Using the Green’s function for the 3D Laplace equation, one can explicitly express the solution to Eqs. (8) and (9) in terms of a convolution (Evans, 2010):

$$\begin{aligned} U_i(\rho, z) &= S_i - \frac{J_i}{4\pi D_i L} \int_{-L/2}^{L/2} \frac{ds}{\sqrt{\rho^2 + (s-z)^2}} = S_i - \frac{J_i}{4\pi D_i L} \int_{-L/2-z}^{L/2-z} \frac{ds}{\sqrt{\rho^2 + s^2}} \\ &= S_i - \frac{J_i}{4\pi D_i L} \ln \left[\frac{1}{\rho^2} \left(L/2 - z + \sqrt{(L/2 - z)^2 + \rho^2} \right) \cdot \left(L/2 + z + \sqrt{(L/2 + z)^2 + \rho^2} \right) \right]. \end{aligned} \quad (10)$$

See Fig. S8a for an example visualization of the above solution. Since we assumed that cells are narrow cylinders, the concentration U_i is approximately constant across most of the cell surface and equal to $U_i(\rho = \rho_o, z = 0)$ (where ρ_o is the cylinder radius), i.e.

$$U_i|_{\text{near cell}} \approx S_i - \frac{J_i}{4\pi D_i L} \ln \left[\frac{1}{\rho_o^2} \left(L/2 + \sqrt{(L/2)^2 + \rho_o^2} \right)^2 \right]. \quad (11)$$

For comparison with the spherical case (section 2.2.2 in the main article), we rewrite Eq. (11) as

$$U_i|_{\text{near cell}} \approx S_i - \frac{J_i}{4\pi D_i R} \cdot \frac{2 \ln \left[E/2 + \sqrt{(E/2)^2 + 1} \right]}{\sqrt[3]{4E^2/3}}. \quad (12)$$

where R is the hypothetical radius of a spherical cell with the same volume as the considered cylindrical cells, i.e. $4\pi R^3/3 = L\pi\rho_o^2$, and the so-called “eccentricity” E is defined as the ratio L/ρ_o . Note the similarity of Eq. (12) to the spherical case, with the addition of the correction factor

$$\beta = \frac{2 \ln \left[E/2 + \sqrt{(E/2)^2 + 1} \right]}{\sqrt[3]{4E^2/3}}. \quad (13)$$

This correction factor, which only depends on the cell eccentricity E , is typically smaller or comparable to 1. In particular, for eccentricities E in the range 2–20, the factor β is roughly within the range 0.75–1.05 (Fig. S8b). Hence, for typical narrow rod-shaped cells the extracellular ${}^x\text{SO}_4^{2-}$ gradients (and hence the microscale reservoir effects) will be similar to spherical cells with an identical cell volume and identical sulfate reduction rates. On the other hand, for much larger eccentricities (i.e. extremely narrow cells, $E \gg 10$) β converges to 0, which means that near-cell sulfate levels and S isotope compositions will be similar to background values, hence eliminating any microscale reservoir effects.

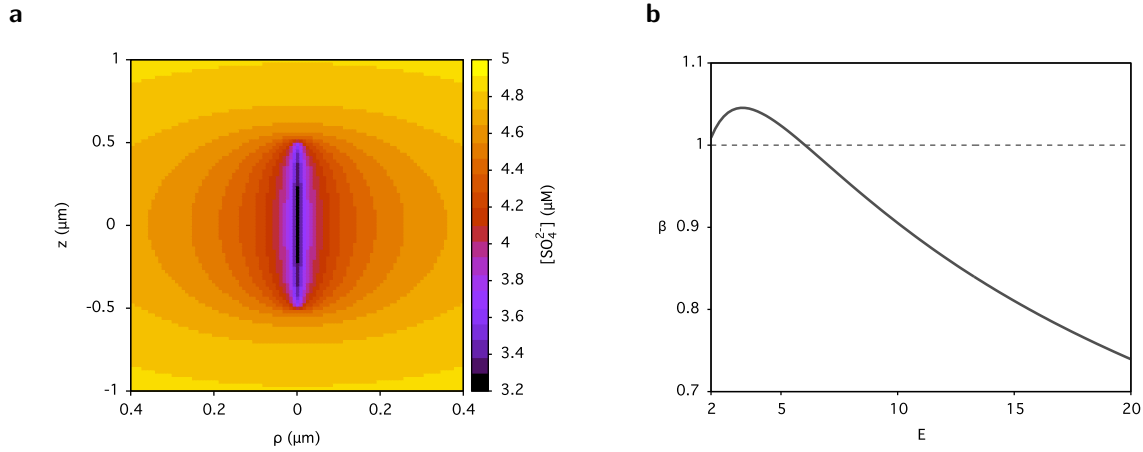


Figure S8: (a) Sulfate concentration around a long, narrow, cylindrical sulfate reducing cell, calculated as described in Supplement S2, Eq. (10). Parameters in this example are: $L = 1 \mu\text{m}$, $D_i = 5.8 \times 10^{-10} \text{ m}^2/\text{s}$, $S_i = 5 \mu\text{M}$, $J_i = 100 \text{ fmol/cell/day}$. (b) Correction factor for the near-cell sulfate concentration for cylindrical cells depending on the eccentricity E , according to Eq. (13).

S3 The Archean ocean water column with variable induced fractionation

In this section we modify the model for S isotope fluxes in the Archean ocean water column discussed in the main article (section 2.5), to include a variable induced fractionation factor, $\tilde{\alpha}$. Specifically, we assume that $\tilde{\alpha}$ depends on the near-cell sulfate concentration \tilde{S} , i.e. $\tilde{\alpha} = \tilde{A}(\tilde{S})$ for some given function \tilde{A} . Similar to the model by Crowe *et al.* (2014), which was based on microscale analyses of Archean pyrites, we assume that $\tilde{\alpha}$ increases linearly from 1.0 to 1.03 at increasing sulfate concentrations until $6 \mu\text{M}$ and saturates at 1.03 for $\tilde{S} > 6 \mu\text{M}$. If microscale reservoir effects are ignored, then $\alpha(z) = \tilde{\alpha}(z) = \tilde{A}(S(z))$, and S_{34} can readily be calculated as the steady state solution to the PDE

$$\frac{\partial S_{34}}{\partial t} = K \frac{\partial^2 S_{34}}{\partial z^2} - \frac{H(z)}{1 + \tilde{A}(z) \cdot (S(z)/S_{34}(z) - 1)}, \quad (14)$$

with boundary conditions

$$S_{34}(z_t) = \frac{r_t S_t}{1 + r_t}, \quad \frac{\partial S_{34}}{\partial z}(z_b) = 0. \quad (15)$$

On the other hand, the incorporation of microscale reservoir effects renders $\tilde{\alpha}(z)$ a function of the near-cell sulfate concentration $\tilde{S}(z)$ which, in turn, depends on the expressed fractionation $\alpha(z)$. Solving the resulting algebraic equations exactly is non-trivial (see Supplement S1). However, when S isotopic differences of thermal diffusion are negligible ($D_{32} \approx D_{34}$, as assumed here) one can approximate \tilde{S} by $S - H/(4\pi RDN)$ and hence calculate $\tilde{\alpha}$ explicitly from the background sulfate concentration $S(z)$:

$$\tilde{\alpha}(z) \approx \tilde{A} \left(S(z) - \frac{H(z)}{4\pi RDN(z)} \right). \quad (16)$$

The expressed fractionation can then be explicitly calculated from $S(z)$, $S_{34}(z)$, $H(z)$ and $N(z)$:

$$\begin{aligned} \alpha(z) &= Z(z) + \sqrt{r(z)\tilde{\alpha}(z) + Z^2(z)}, \\ Z(z) &= \frac{H(z)}{S(z)} \cdot \frac{(1 + r(z))}{8\pi RDN(z)} [1 - \tilde{\alpha}(z)] + \frac{1}{2}(\tilde{\alpha}(z) - r(z)), \\ r(z) &= \frac{S_{34}(z)}{S(z) - S_{34}(z)}. \end{aligned} \quad (17)$$

Using Eq. (17) in the PDE (14), and using the same model parameters as in the main article, eventually yields the steady state isotopologue ratio and expressed fractionation profiles shown in Fig. S9. Note

that both macroscale and microscale reservoir effects are significantly weaker than in the model analyzed in the main article (Fig. 5), where the fractionation factor $\tilde{\alpha} = 1.03$ was fully induced by the cells even at low sulfate concentrations at depth.

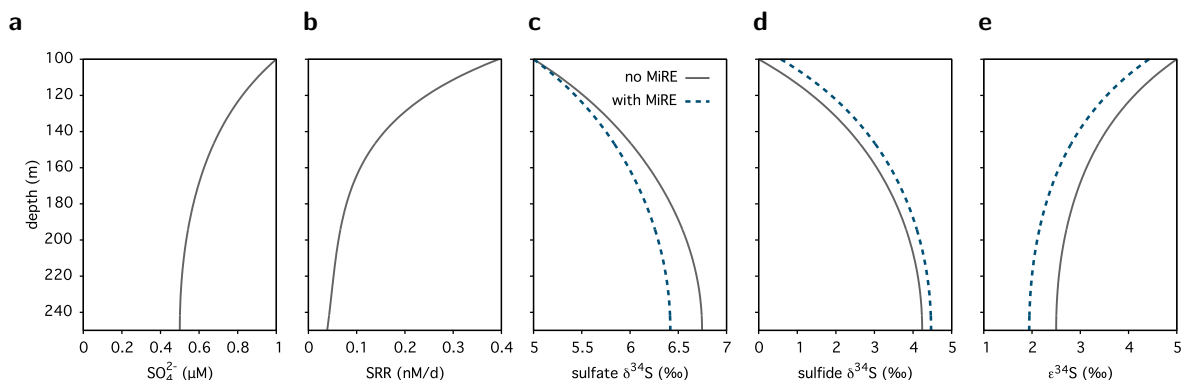


Figure S9: 1D reaction-diffusion modeling of S isotope fluxes in the Archean ocean water column at steady state and using a variable induced fractionation ($1.0 \leq \tilde{\alpha} \leq 1.03$), as described in Supplement S3. (a) Sulfate concentrations, (b) sulfate reduction rates, (c) sulfate S isotope composition, (d) exported sulfide S isotope composition, (e) expressed S isotope fractionation (w.r.t. the background sulfate S isotope composition). Continuous and dashed curves show model predictions without and with the microscale reservoir effect (MiRE), respectively. At the top, sulfate was fixed at $1 \mu\text{M}$ and sulfate $\delta^{34}\text{S}$ was set to 5‰ (Shen *et al.*, 2001).

References

- Boudreau B.P. (1997) *Diagenetic models and their implementation; modelling transport and reactions in aquatic sediments*. Springer.
- Crowe S.A., Paris G., Katsev S., Jones C., Kim S.T., Zerkle A.L., Nomosatryo S., Fowle D.A., Adkins J.F., Sessions A.L. *et al.* (2014) Sulfate was a trace constituent of Archean seawater. *Science* **346**, 735–739.
- Evans L. (2010) *Partial Differential Equations*. Graduate Studies in Mathematics. American Mathematical Society, 2nd edition.
- Garrity G. (2005) *Bergey's Manual of Systematic Bacteriology: Volume 2 : The Proteobacteria*. Bergey's Manual of Systematic Bacteriology. Springer US.
- Habicht K.S., Gade M., Thamdrup B., Berg P. and Canfield D.E. (2002) Calibration of sulfate levels in the Archean ocean. *Science* **298**, 2372–2374.
- Haglund A.L., Törnblom E., Boström B. and Tranvik L. (2002) Large differences in the fraction of active bacteria in plankton, sediments, and biofilm. *Microb. Ecol.* **43**, 232–241.
- Huber R., Rossnagel P., Woese C.R., Rachel R., Langworthy T.A. and Stetter K.O. (1996) Formation of ammonium from nitrate during chemolithoautotrophic growth of the extremely thermophilic bacterium *Ammonifex degensii* gen. nov. sp. nov. *Syst. Appl. Microbiol.* **19**, 40–49.
- Iversen N. and Jørgensen B.B. (1993) Diffusion coefficients of sulfate and methane in marine sediments: Influence of porosity. *Geochim. Cosmochim. Acta* **57**, 571–578.
- Keller K.L., Rapp-Giles B.J., Semkiw E.S., Porat I., Brown S.D. and Wall J.D. (2014) New model for electron flow for sulfate reduction in *Desulfovibrio alaskensis* G20. *Appl. Environ. Microbiol.* **80**, 855–868.
- Lambert I.B., Donnelly T.H., Dunlop J.S.R. and Groves D.I. (1978) Stable isotopic compositions of early Archaean sulphate deposits of probable evaporitic and volcanogenic origins. *Nature* **276**, 808–811.

- Llobet-Brossa E., Rabus R., Böttcher M.E., Könneke M., Finke N., Schramm A., Meyer R.L., Gröttschel S., Rosselló-Mora R. and Amann R. (2002) Community structure and activity of sulfate-reducing bacteria in an intertidal surface sediment: a multi-method approach. *Aquat. Microb. Ecol.* **29**, 211–226.
- Nauhaus K., Albrecht M., Elvert M., Boetius A. and Widdel F. (2007) In vitro cell growth of marine archaeal-bacterial consortia during anaerobic oxidation of methane with sulfate. *Environ. Microbiol.* **9**, 187–196.
- Richter F.M., Mendybaev R.A., Christensen J.N., Hutcheon I.D., Williams R.W., Sturchio N.C. and Beloso Jr. A.D. (2006) Kinetic isotopic fractionation during diffusion of ionic species in water. *Geochim. Cosmochim. Acta* **70**, 277–289.
- Robert F. and Chaussidon M. (2006) A palaeotemperature curve for the Precambrian oceans based on silicon isotopes in cherts. *Nature* **443**, 969–972.
- Shen Y., Buick R. and Canfield D.E. (2001) Isotopic evidence for microbial sulphate reduction in the early Archaean era. *Nature* **410**, 77–81.
- Ueno Y., Ono S., Rumble D. and Maruyama S. (2008) Quadruple sulfur isotope analysis of ca. 3.5 Ga Dresser Formation: New evidence for microbial sulfate reduction in the early Archean. *Geochim. Cosmochim. Acta* **72**, 5675–5691.
- Vos P., Garrity G., Jones D., Krieg N., Ludwig W., Rainey F., Schleifer K. and Whitman W. (2011) *Bergey's Manual of Systematic Bacteriology: Volume 3: The Firmicutes*. Bergey's Manual of Systematic Bacteriology. Springer New York.
- Widdel F. and Bak F. (1992) Gram-negative mesophilic sulfate-reducing bacteria. In *The Prokaryotes* (eds. A. Balows, H. Trüper, M. Dworkin, W. Harder and K.H. Schleifer), Springer New York, pp. 3352–3378.
- Wing B.A. and Halevy I. (2014) Intracellular metabolite levels shape sulfur isotope fractionation during microbial sulfate respiration. *Proc. Natl. Acad. Sci. USA* .